Improved Environmental Operation of Alcohol Breathalyzers with Functionalized Graphene Nanocomposite Membranes

by

Jared Lenos

A thesis
presented to the University of Waterloo
in fulfillment of the
thesis requirement for the degree of
Master of Applied Science
in
Chemical Engineering (Nanotechnology)

Waterloo, Ontario, Canada, 2016

I hereby declare that I am the sole author of this thesis. This is a true copy of the thesis, including any required final revisions, as accepted by my examiners.

I understand that my thesis may be made electronically available to the public.

Abstract

Driving under the influence of alcohol is prohibited or restricted in almost every country on the planet. In Canada, a Blood Alcohol Content (BAC) of 0.08 g dL^{-1} results in a Criminal Code offense and vehicle impoundment. Critical to this charge and its associated consequences is the technology assessing alcoholic content. Modern police forces use handheld or stationary breath analysis tools to evaluate alcohol ingestion. In order for punitive measures to be enforced, the reliability and accuracy of breathalyzers must go without question. However, methods employed to improve the reliability of modern sensors waste significant energy to control the test environment; namely humidity and temperature of the test cell. Through a more thorough investigation of the parameters which govern an ethanol fuel cell sensor (FCS) response, we can design a testing cell itself which is insensitive to its environment while improving the specificity.

Modern FCS are based on acid-soaked poly-vinyl chloride (PVC) with a platinum on carbon catalyst hot-pressed directly to the membrane interface. More recently, Nafion by Dupont has been investigated as an alternative, strongly conductive and stable membrane material. Both of these fall prey to water loss, limiting their response to varied environmental conditions and requiring frequent calibration. This project designs and tests engineered nanocomposite membranes to enhance the reliability of the FCS response. Increasing the thickness of Nafion nanocomposite membranes correlated with improved sensor responses. Integration of 5 wt% 1:1 ratio of sulfonic-acid functionalized nanoporous silicon dioxide to functionalized graphene oxide in Nafion best enhanced a FCS response in low humidity, showing stability even at 100 days in a low humidity environment.

Acknowledgments

I would like to express my deepest gratitude to my supervisor, Dr. Zhongwei Chen who provided the space, enthusiasm and industry connections to really bring this project to life and keep it commercially-minded. I am also deeply grateful to Gaopeng Jiang, without whose guidance and support this project would have stalled long ago. Further, the expertise and advice of other lab members such as Abel Sy, Dr. Hadis Zarrin, Zhang Jing, Guihua Liu, Gregory Lui, and Alicia Veileux was invaluable. I will also mention Dr. Siamak Farhad for his role in the instigation of this research.

I must also thank the many machine shop technicians, the Science electronics shop operator and the 3D print center co-op students in providing design feedback and performing some technical work on behalf of this project.

Finally, I express immense gratitude to my loving family and to Dilara Yilman for daily supporting me with love and encouragement in pursuit of emerging technology.

Dedication

I would like to dedicate this Thesis to Dilara Yilman, who has more love than the surface area of pristine graphene.

Table of Contents

List of Tables

List of Figures

Chapter 1

Introduction

1.1 Background

The April 2016 ruling by Ontario Court Justice Elinore Ready acquitted a driver who failed a roadside breath test, calling into question the integrity of the device. The expert witness, Ben Joseph, had determined that the instrument's history showed inaccurate results, poor maintenance and other failures. Further, he testified that all breathalyzer models used in Ontario lack an established error rate, meaning that there is no statistical confidence in a given breath-test reading. The U.S.-based manufacturer defended itself by saying, "CMI stands behind the accuracy and integrity of its breath testing instruments." The Crown has filed an appeal[1] to overturn the ruling.

As thousands of impaired-driving sentences are meted out yearly across Canada, including criminal offenses, the reliability and accuracy of the alcohol breath analysis machine must be beyond reproach. Environmental conditions may exist which call into question the validity of a given test such as the presence of ambient alcohol, how recently alcohol has been consumed or even whether the officer administering the test performed his duties knowledgeably and adequately. Irrespective of these conditions which cause deviation from the true state of inebriation, there must be no doubt that the alcohol response provided is

Table 1.1: Effect of Ethanol on humans based on BAC[4]

BAC g dL^{-1}	Typical Effect
0.02 to 0.03	Noticeable cognitive changes
0.08 to 0.20	Person obviously intoxicated, delirium
0.25 to 0.35	Loss of consciousness
> 0.45	Severe coma and death

accurate.

An understanding of evidential breath-testing and how it relates to your Blood Alcohol Content (BAC) is required before considering chemical analysis. BAC has been well studied and the effect of alcohol on the human body has been categorized into several ranges (Table 1.1)[2–4] although these general symptoms are not suitable determinants for inferring a patient's BAC.[5] General concerns about the invasive nature of blood testing led to developments in non-invasive techniques including breath-testing. It is considered to be a good estimate of BAC through the assumption that ethanol diffusing into and out of tracheal mucous was recently in equilibrium with alveolar blood.[6] Simply put, the air mixture within your lungs is considered to be the gas-equivalent of your blood weighted by volatility. The gas-liquid equilibrium of blood alcohol and lung air can be calculated using Henry's Law (Eq. 1.1) where R is the gas constant, T is the temperature k_{eq} is known equilibrium constants.[7] The exact calculation using the citation listed results in a breath to blood partition ratio ($k_{e/p}$) of 2298. Gas chromatography studies directly measuring the ethanol concentration in air over a known concentration in voluntary blood samples report values of 2157 $\pm$ 9.6 for men, and 2195 $\pm$ 10.9 for women.[8] Generally a partition ratio of 2100 is accepted.[9–12] In Canada, BAC is reported in grams of ethanol per 100 mL of blood. To achieve this, a simple conversion is applied (Eq. 1.2) where $M(EtOH)$ is the molar mass of ethanol.

$$BAC = BrAC * k_{eq}RT \approx 2100 * BrAC \tag{1.1}$$

$$\frac{g}{dL} = \frac{BAC * M(EtOH)}{10} \tag{1.2}$$

Breath-testing devices are considered evidential in Canada when they match or exceed the conditions set out by the Canadian Society of Forensic Science Alcohol Test Comittee[13] with an ISO/IEC 17025 accreditation. Some examples of requirements is that the mean result of thirty consecutive analysis at each concentration must be within 5% of the target value; and that after a minimum of 50 analyses using no fewer than ten human subjects with a BAC between 50 to 150 mg per 100 mL, a device must be at least as accurate and precise as near-simultaneous tests with an Approved Instrument. These conditions must continue to be satisfied at yearly intervals and maintenance logs kept for each Approved Instrument including preventative maintenance, modifications, replacements and all inspections. Due to increases in test requirements, several methods originally used to detect breath alcohol content have been phased out.

1.2 Breathalyzer History

Breathalyzer technology, the modern name for portable breath-analysis, has changed significantly since its inception in 1954.[14] Initially, a chemical reaction where a breath sample is bubbled through a mixture of sulfuric acid, potassium dichromate, water and optionally silver nitrate will cause the dichromate ion to change color when it reacts with CO_2.[15] A photocell compares this colour change with unreacted fluid, producing an electric current to indicate ethanol concentration. This technology is still sold as a cheap personal alcohol detector, however a short shelf life and poor reliability have long pushed it from the evidential market.[16]

Based on the observation that ethanol natively absorbs infrared light, several versions of non-portable and more recently, portable IR sensors have been manufactured. An end-expiratory air sample is introduced into a chamber and the resulting measurable change in IR ($\lambda = 3.46$ µm) output indicates the gas-concentration.[17] This effect is perfectly linear

between concentration and response allowing for simple calculation of ethanol content.[18] These are the type of breath-detectors found as table-top units in police stations, exhibiting high accuracy and requiring frequent calibration. Portable versions tend to be large and heavy, costing in excess of $1000 per unit.[4]

Semiconductor sensors use a bead of heated metal oxide and a small standing current to detect alcohol. When the gas comes into contact, it changes the surface resistivity and therefore the current response.[19] Major concerns are with the specificity of this resistive change, its non-linear response profile in changing concentrations and current drift as the oxide ages. Typically semiconductor oxide sensors are used as a detector of the presence of alcohol instead of concentration.

With increased interest in fuel cells as viable power sources for vehicles and small devices, innovations in fuel cell technology allow direct alcohol fuel cells (DAFCs) to consume ethanol.[20,21] Instead of harnessing the energy produced it can be characterized to determine the number of ethanol molecules present. This type of fuel cell, called a fuel cell sensor (FCS), has been widely employed in portable breathalyzer technology. The response of an FCS to a breath sample has been shown to be specific to ethanol, precise and stable during calibration testing. The major drawback is a need for frequent recalibration within every 1000 tests as the electrochemical response gradually diminishes. The majority of high quality consumer and evidential portable breathalyzers use this characterization method due to their accuracy, small size and relatively low cost. However, low quality and cheap breathalyzers also employ ethanol FCSs which demonstrate poor accuracy and consistency. Like many other fields, the choice of material composition, manufacturing process and standard test environments provides degrees of difference in the performance of a FCS-based breathalyzer. Through a more complete understanding of the principles governing the response of a fuel cell sensor, especially related to its long-term degradation, we predict future generations without the requirement for calibration will emerge.

1.3 Project Collaboration and Confidentiality

In August 2013, Alcohol Countermeasure Systems (ACS) partnered with the University of Waterloos Applied Nanomaterials and Clean Energy Laboratory (ANCEL) with the aid of a National Sciences and Engineering Research of Canada (NSERC) grant, and later an Ontario Center of Excellence (OCE) grant. The focus of this partnership was in developing the next-generation of ethanol sensors, especially membrane and catalyst development. A non-disclosure agreement had been in place from the onset, marking the materials and content within as confidential intellectual property (IP) with the aim of establishing a patent following successful experimentation.

1.4 Objective

The objective of this research is to remove any humidity and temperature dependent response within a fuel cell sensor. Specifically, functionalized graphene nano-composite membranes are proposed as a viable candidate. Towards this end and with the collaboration of ACS focus was on:

- Building and maintaining consistent testing conditions
- Development and investigation of functionalized nano-materials into Nafion
- Long-term degradation results in varying humidity and temperature environments

1.5 Organization of Thesis

There are 5 Chapters detailed in this thesis. The second chapter consists of a review of fuel cell fundamentals, highlighting the specific components that most directly affect a FCS response. The third chapter is an overview of the specific methods employed in synthesis, preparation, testing and characterization of a FCS. This chapter includes a significant section on the design and creation of an automated testing station. The fourth

chapter discusses all relevant results, sample characterization and makes several comparisons between these. The final chapter is a conclusion, putting all the research conducted into perspective and briefly highlighting future steps to take.

Chapter 2

Alcohol Fuel Cell Sensor Review

2.1 Introduction and Market

There are several challenges facing ethanol fuel cell sensors (FCSs). To be successful, a new breathalyzer sensor must be cost effective, insensitive to its environment, have high performance and quick response and also display unparalleled durability and reliability. These characteristics have historically differentiated evidential-grade portable breathalyzers from personal ones, but if made cost-effective there is a significant market at the ready. Research by Markets and Markets (Figure 2.1) showed in 2012 that alcohol detection was roughly half of all breath analysis, with a market over 200 million USD. Their report predicted a compound annual growth rate (CAGR) of 41.3% to 4.5 billion USD in 2019.[22] Their later 2014 report put the global market at 479.3 million and updated the CAGR to 26.3%, cutting their 2019 predicting to 1.54 billion.[23] Two reports by Technavio estimated the CAGR at 44.37[24] and 41.57[25] between 2013-2018, citing "one of the major challenges faced by the market is the inaccurate results that are sometimes provided by breath analyzers".[25]

In the scope of the total project the required approach is two-fold. First, development of improved ion conducting membranes for reliable long-term operation. Second,

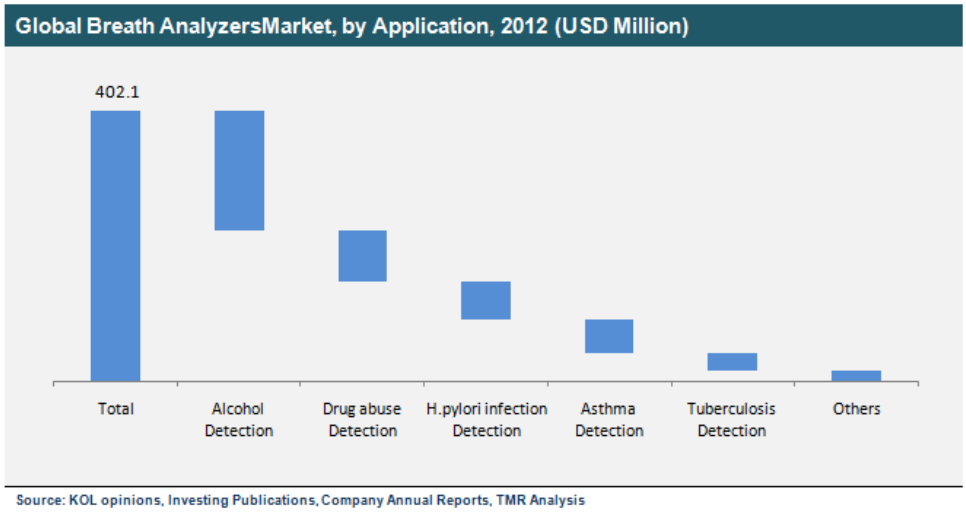

Figure 2.1: Global Breath Analyzer Market by Application - 2012 (USD) Millions[22]

catalytic improvement to significantly decrease the cost and improve specificity. Several types of novel electrolyte membranes were proposed focusing on two segments; polymer nanocomposite membranes and morphologically modified polymers. In this first branch, functionalized graphene oxide,[26–29] silicon dioxide,[30–32] titanium dioxide,[33–35] zeolites[36–38] and other nanostructured materials could be integrated into a polymer structure to provide increased overall sulfonic functionalization. In the second branch, membranes based on polymers containing PFSAs,[39,40] porous polybenzimidazole[41–44] or porous poly-vinyl alcohol[45,46] hold potential for environmental insensitivity. All the testing performed here focuses on that first zone: investigating functionalized graphene nanocomposite polymer membranes.

2.2 Principle of Operation

A fuel cell sensor (FCS) is fabricated from several components as shown generally in Figure 2.2. The anode and cathode are terminals for a circuit to connect to, whereby electrons produced from the electrochemical reaction can be consumed or measured. These

can be any conductive material, in most FCS being a carbon cloth or carbon paper material which permits gas permeation. The inside edge of both the cathode and anode is coated with a catalyst to enable the electrooxidation of ethanol and produce electrons. The separator is electrically non-conductive, forcing any produced charge into an external circuit while allowing ions to pass through to complete the reaction.

The anodic reaction involving ethanol (Figure 2.3) results in a complex mixture of products including acetic acid, acetaldehyde and carbon dioxide via the reactions 2.1, 2.2 and 2.3 respectively. At ambient conditions the major product is acetic acid.[47–49]

$$C_2H_5OH + H_2O \longrightarrow CH_3COOH + 4\,H^+ + 4\,e^- \tag{2.1}$$

$$C_2H_5OH \longrightarrow C_2H_4O + 2\,H^+ + 2\,e^- \tag{2.2}$$

$$C_2H_5OH + 3\,H_2O \longrightarrow 2\,CO_2 + 12\,H^+ + 12\,e^- \tag{2.3}$$

The protons (H^+) migrate through the separator, in this case called a proton exchange membrane (PEM), to reach the cathodic compartment. At the cathode, the electroreduction of oxygen produces water (Eq. 2.4). From this reaction schema it can be observed that ethanol oxidation always involves the participation of water, such that both chemisorption of the alcohol and activation of the water molecule will constitute a good electrocatalyst.

$$O_2 + 4\,H^+ + 4\,e^- \longrightarrow 2\,H_2O \tag{2.4}$$

2.3 Catalyst

Platinum is recognized as the most active catalyst towards ethanol oxidation. Significant research has already gone into metal and non-metal additives to further enhance its interaction with ethanol.[50–52] For the complete oxidation (Eq 2.3) it is necessary to break the C-C bond within the ethanol backbone to reform into carbon dioxide.[21] This step

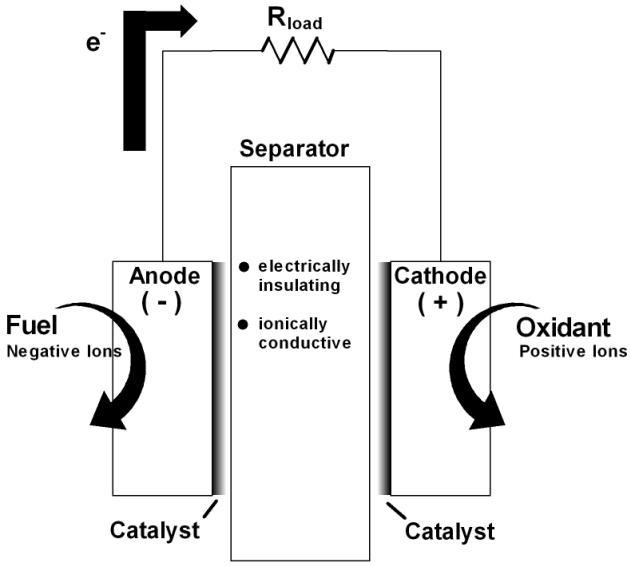

Figure 2.2: Fuel cell sensor general schematic

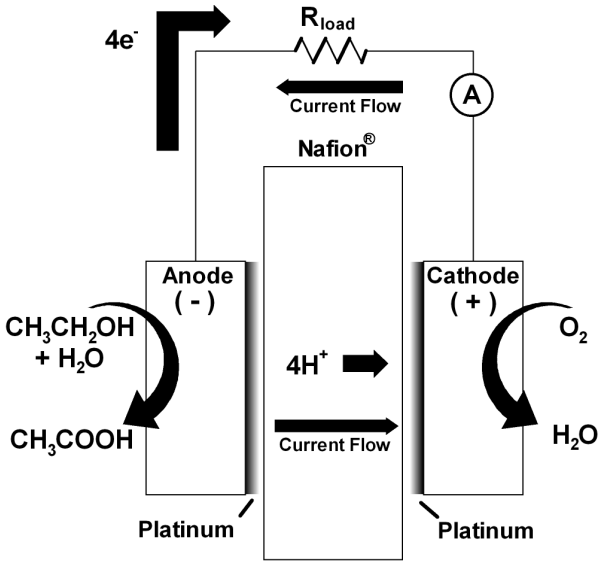

Figure 2.3: Ethanol reaction and current flow

requires significant activation energy and is rarely observed at ambient temperatures. It should be noted that intermediates are also formed during oxidation, and if carbon monoxide (CO) molecules adsorb to the catalytic platinum surface it will experience catalytic 'poisoning' where an irreversible bond prevents further catalysis at that site.[48] Ambient oxidation of ethanol on platinum is assumed to be a four electron process producing acetic acid (Eq. 2.5) and is well supported in literature.[53,54]

$$C_2H_5OH + O_2 \longrightarrow CH_3COOH + H_2O \tag{2.5}$$

2.4 Membrane

Besides the catalyst, an integral component of the fuel cell sensor is the separator or PEM. The most well known proton conducting membrane is a perfluorosulfonic acid (PFSA)-based polymer called Nafion ™produced by Dupont (Fig. 2.4). The protons are driven across this membrane by a concentration gradient, moving from the anode toward

the cathode[55,56] and limited by the PEM diffusivity.

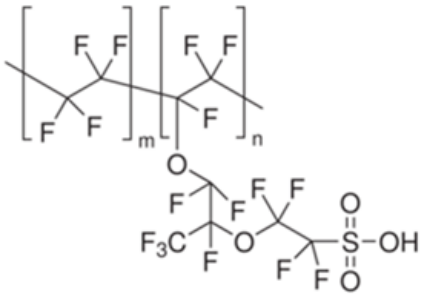

Figure 2.4: Structure of Nafion ™

Although the *de-facto* membrane and catalyst appear to be well-defined for the proton exchange membrane fuel cell sensor (PEMFCS), some concerns arise which lead to a search for more suitable materials. The principle concern in Nafion ™based cells is the strong dependence of Nafion ™on water molecules to drive proton conduction.[57] As the membrane is exposed to ambient conditions following immersion during membrane synthesis, it slowly loses proton conductivity.[58] This phenomenon also indicates that the membrane response will vary due to uncontrolled environmental conditions. A secondary concern is the apparent ability for Nafion ™to permit ethanol cross-over, where ethanol molecules reach the cathodic side and dampen the electronic response by providing electrons there.[47,59–61]

Some companies have refrained from solid state electrolytes and continue to use acid-soaked polymers employing a membrane-bound liquid electrolyte.[62] A "mosaic type" of sintered poly-vinyl alcohol granules is bonded using polyvinyl chloride.[63] This sheet-like matrix forms a polymeric support for absorbing sulfuric acid, creating the cheap and popular commercial electrolytic membrane. However, it exhibits a very strong dependence on temperature and humidity,[64,65] such that a degree or two will affect the electronic response baseline by more than 10%. To combat this, a heating diode is placed in tandem with the cell and the sensor response is not taken until the cell has warmed up to a well-calibrated temperature. This preventative measure accelerates water loss from the acid electrolyte, prompting the need for frequent recalibration and potential sensor replacement in com-

mercial units.

In general, any solid electrolytes has to satisfy the following conditions:

- high ionic conductivity
- low electronic conductivity
- high stability in reducing and oxidizing conditions
- low fuel cross-over
- reasonable mechanical strength

Several additional desirables are simplified design and assembly, lower corrosion and no danger of electrolytic spill.[49] Many variations of solid-state membranes have been tested in fuel cell systems, such as functionalized nano-composite membranes,[21,26,36,66–71] sulfonated polymeric membranes[43,72–78] as well as a large subset of aqueous and ceramic electrolytes.[20,79–81] To-date, very few of these have been also applied to a fuel cell sensor, specifically with temperature and humidity insensitivity in mind. This project aims to investigate and expand on that principle with the direct commercial application in mind.

2.4.1 Membrane Electrode Assembly

A FCS broadly covers many components including the fuel inlet, gas chamber and sensor housing as well as electrode contact pads (Fig. 2.5). From a materials perspective we care about the electrochemical "heart" called the membrane electrode assembly (MEA). This consists of five elements: the anode gas diffusion layer, the anode catalytic layer, the electrolytic membrane, the cathode catalytic layer and finally the cathode gas diffusion layer (Fig. 2.6). The diffusion layer is required to permit the gaseous fuel and water to come into contact with the catalyst. It also acts as a conductor to remove electrons produced in the reaction. The catalyst layer is exactly at the interface of the solid proton conducting electrolyte and diffusion layer, such that the electrons and protons produced are simultaneously conducted. The membrane is the separator between the anode and cathode

as well as the proton carrier, and is typically acid soaked or acid functionalized to enhance proton mobility. The MEA is fabricated by pressing pre-catalyst-coated diffusion layers onto the membrane at elevated temperature, or by preparing a catalyst-coated-membrane (CCM) and hot-pressing the diffusion layer after.

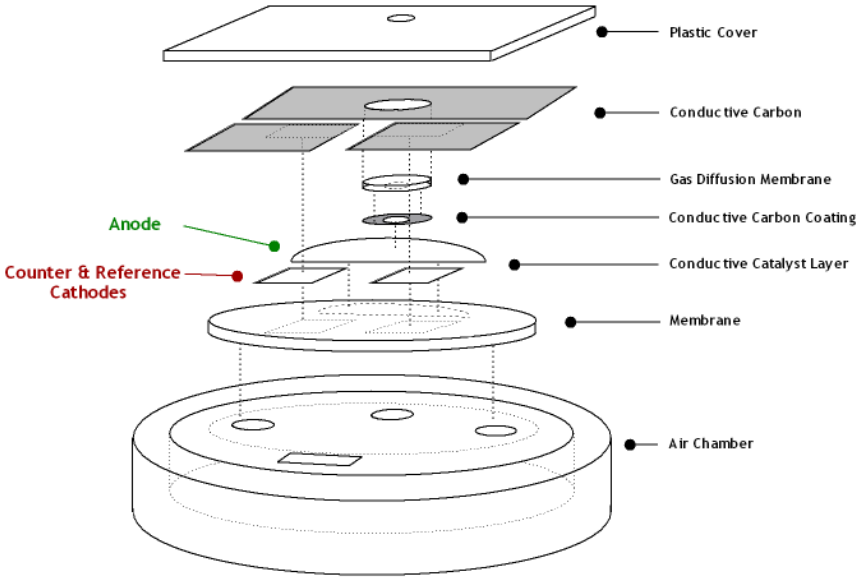

Figure 2.5: Schematic of a commercial fuel cell sensor

2.4.2 PFSA Membrane

Nafion ™has a backbone structure which is derived from polytetrafloroethylene (PTFE) copolymerized with polysulfonyl fluoride vinyl containing pendant sulfonic acid (SO_3H) groups. As a cation exchanger, the firmly bound hydrophilic SO_3^- radicals associate with H^+ counter ions to be charge neutral. When water is present, these counter ions are solublized to form complexes such as hydronium (H_3O^+) which can be transported to enable ionic (proton) conductivity.[82] The PTFE backbone enhances the mechanical properties, while remaining hydrophobic to create distinct water-free and water-full phases. There is significant research done to study the structure of Nafion ™, and the accepted theory is that

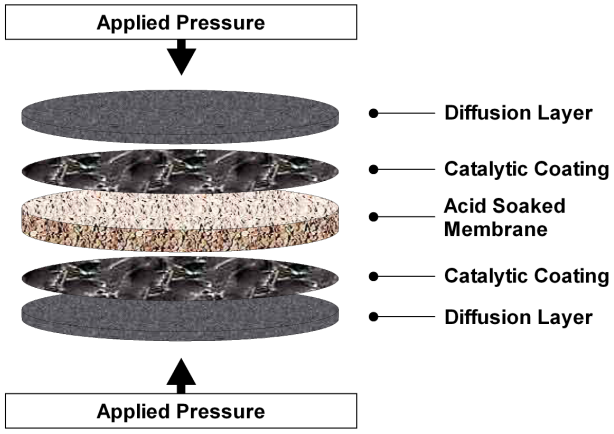

Figure 2.6: Typical membrane electrode assembly (MEA) in a FCS

the free volume space in Nafion ™aggregates into connected nanometer sized pores lined with sulfonic acid groups.[83,84] The presence of water therefore creates a 'semi-liquid electrolyte' state where ions are transported through these interconnected pockets of sulfonic groups. The resulting conductivity is comparable to that of a liquid electrolyte, except that the polymer is a solid with no liquid phase unless excess water is present. This conductivity, adding to good mechanical strength, chemical stability and gas permeability has made it ubiquitous in fuel cell and sensor applications.

Additionally, Nafion ™is well known for its ability to absorb water. Volume measurements typically report swelling of more than 20% in liquid, and 14% in humidified air.[85] Fuel cell stacks integrate humidity into fuel lines of H_2 and O_2 in order to maintain membrane hydration. In the specific case of breathalyzer technology, each human breath contains humidified air - making Nafion ™attractive in terms of regaining water content due to its high affinity to absorb water. Still, several researchers have demonstrated the variability of a gas sensor response dependent on the relative humidity (RH)[86,87] marking it as impractical for measurements in ambient air where a wide variety of RH is possible.

2.4.3 Ion Conduction

Conductivity is the ability to allow charge movement in the presence of an electric field. It is influenced by two major factors: how many charge carriers are present to transport charge, and the mobility of those carriers inside the material. These two can be characterized by the carrier concentration c_i and the carrier mobility u_i. The rate at which ions can be carried through a membrane is dependent on its material properties. The effectiveness of the movement of ions is characterized by the material diffusivity D

$$D = D_o e^{\frac{-\Delta G_{act}}{RT}} \tag{2.6}$$

where D_o reflects how often ions attempt to move, ΔG_{act} is the activation barrier, R is the gas constant and T is temperature (K). The overall mobility of ions in a solid electrolyte, which is our conducting medium of interest, is given by

$$u_i = \frac{|z_i|FD}{RT} \tag{2.7}$$

where z_i denotes the charge per carrier (protons have a charge of 1), F is Faraday's constant, R is the gas constant and T is the temperature (K). The equation for conductivity can be shown to be

$$\sigma = |z_i|Fc_iu_i = \frac{c_i(z_iF)^2D}{RT} \tag{2.8}$$

Nafion ™demonstrates an ion diffusivity of about $1 * 10^{-8}$ m^2 s^{-1},[88] and ion carrier concentration of about 1 kmol m^{-3}.[89] It should be noted that liquid electrolytes have a typical ion carrier concentration 10x higher than polymer electrolytes, making this field highly competitive.

It is easy to note from these equations that our conductivity is an exponential relationship dependent on temperature, and we can derive

$$\sigma T = \sigma_o e^{\frac{-E_a}{kT}} \tag{2.9}$$

where σ_o represents a reference conductivity and E_{act} the activation energy in eV mol^{-1}. Most polymer and crystalline ion conductors follow this model, including PFSA polymer membranes.[90,91]

2.5 Operation of a Breath Sensor

Throughout the duration of this project, full cell realistic tests were performed in amperometric mode. A conventional response curve is shown in Figure 2.7, highlighting the characteristics of a single fuel cell sensor when fuel is injected. Typically, 0.5 mL of a mixture of humid air and ethanol at a known concentration is drawn into the fuel cell sensor by a solenoid-actuated sampling pump.

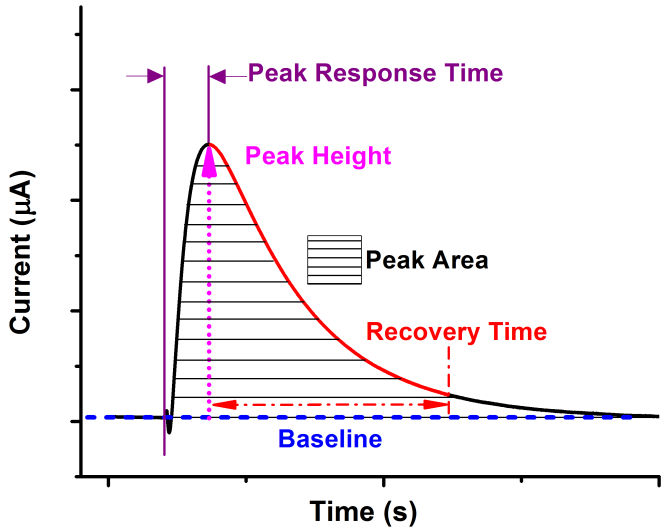

Figure 2.7: Current vs time response of a conventional fuel cell sensor and important parameters taken from it

The fuel and water vapour comes into contact with one side of the MEA, where the platinum catalyst facilitates the oxidation reaction to acetic acid, releasing a number of electrons and protons. A digital meter is monitoring the current response in a low-resistance

loop to produce the curve depicted. The indicative response can be analyzed for certain values, in order of importance being the

- Curve Integral (µA s) and stability
- Curve peak value (µA)
- Curve time-to-peak value (sec)
- Curve Recovery Time (sec)
- Baseline (nA)

Each is explained in the subsections below.

2.5.1 Response Integral

The curve integral is extremely important as through it we can directly measure the number of electrons transferred, and therefore have an idea as to the concentration of fuel present. Further, it has been shown that the curve integral responds linearly to fuel concentration, meaning that a well-calibrated device will be accurate for a wide range of values instead of specific or fitted points.[49,92]

2.5.2 Response Height

The peak value is a good indicator of degradation. As the membrane increases in resistivity the ohmic losses of the whole circuit is affected. This means that although the integrated current response is maintained, due to the same number of ethanol molecules being reacted the actual response curve may be "slumped" and take more time to return to its baseline. Therefore, the maximum current response provides a quick way of detecting changes in the speed response of the cell to a given injection even before the integral can be measured. Further, if the peak value is sustained consistently by a sample it can replace the integral as a much faster and computationally inexpensive measure of ethanol concentration.

2.5.3 Response Speed

The time-to-peak value acts similarly to the peak value in predicting sensor degradation. However, it also provides an important metric for retaining user-friendliness. When considering any new material as a candidate for a commercial application, the concept of usability must also be maintained. A precise sensor that takes 15 minutes to provide a response is less desirable than a 5 second sensor with reasonable accuracy.

2.5.4 Response Recovery

The curve recovery time indicates how long it takes the cell to consume the provided fuel before another test can be run. The longer this runs on, the less reliable a second test is going to be if taken in a real-life situation. Many evidential breath-testers are tested for their repeatability and if the recovery time is too large, some remaining fuel will be integrated into the next test, providing a source of error.

2.5.5 Response Baseline

The baseline is of interest as it indicates if the cell is at equilibrium or not. For instance, for hydrogen fuel cell operation it is essential to know how water content varies across a membrane. As protons travel, they drag water and fuel molecules with them. This is called electro-osmotic drift when referring to water, and cross-over contamination when related to fuel. Since conduction is related to the water content, this means that the performance of the cell suffers during the reaction depending on the current rate. In fuel cell sensors this phenomenon is non-existent due to the fraction of ethanol consumed and water being produced, however if the anode is exposed to a low-humidity environment for long enough, water loss will create a concentration gradient. A standing current will be observed as protons and water molecules exist in disequilibrium. This drift is negated by testing in either a well maintained environment, or if the sampling time is short enough such that there is no significant effect on the integral of the curve.

Stability of a given response can be characterized by either long-term or short term fluctuations. The cause of a drift in the baseline, or changes in the signal magnitude are poorly characterized. All that is known is that temperature fluctuation, operation and extreme humidities for long periods of time, catalyst degradation and fouling and electrolyte contamination all contribute to changes in the elemental operation of a fuel cell sensor. Despite this, traditional fuel cell sensors last several years and still retain valid analytical performance.[82]

2.6 Response Characterization

2.6.1 Sensitivity

We can determine sensitivity by finding the slope of sensor response verses fuel concentration. In measuring the current area, we obtain a qualitative and linear relationship. Generally, the lower detection limit (LDL) is where the concentration value is at least 3 times larger than the sampling noise. There are several factors which affect the signal at very low concentration, being mass transport limitations, poor electrocatalytic activity, analyte solubility and mobility, the physical geometry of the sensor and even the operating method if using any filter or air scrubber membranes.[93] It is not limited by the signal due to advances in modern electronics, however the background current noise limits most detection to a 1 parts-per-million (ppm) level. This background current can be due to:

- Electrolytic impurities, slow oxidation or reduction of solvent
- Electrode corrosion, such as a passivating layer
- Diffusion of reactant or reaction products

2.6.2 Selectivity

The selectivity of a sensor is quantified as the ratio of signal for the target analyte compared to that of any other species that may be present. As platinum is electroactive towards many species of alcohols, there is a high chance that more than simply the fuel of choice is producing or consuming charged species and thereby affecting the current response. Interference in the desired measurement should be either known and predictable, or insignificant. In a given breath sample there are more than 200 known interferents as well as additional elements such as hydrogen from smokers, alcohol due to mouthwash and a variety of other volatile species that are at equilibrium in the human body.[94]

2.6.3 Accuracy

As a fuel cell sensor response does not ensure 100% conversion of the ethanol sample introduced, accuracy relates a measurement to a known "true" value and computes the reliability based on extrapolation or interpolation at another known concentration. Test precision is the repeatability or deviation of a given measurement which must fall within industry standards of 5%.[13] In the case of breathalyzer samples, standard solutions must be very carefully composed in order to obtain that "true" value consistently. Instrument and measurement precision should also be known. Background noise will affect the current response, however signals that are 10-100 times larger than the background current should provide a precision within 1%.[82,95] Accuracy is measured by looking at the lack-of-fit (LOF) when conducting linearity tests. Precision is measured by performing repeat experiments and calculating the standard deviation of the integrated current area.

Chapter 3

Methods and Procedures

3.1 Nanomaterials Synthesis

3.1.1 Graphene Oxide

Graphene is an exciting material especially concerning its theoretical surface area (2630 m2 g-1).[96] Unfortunately, it is difficult to find a use for graphene in fuel cell sensor membranes as it is a poor ion conductor and has high intrinsic electronic conduction. In order to improve ionic transport and take advantage of the very large surface area, graphene needs to be chemically functionalized. Graphene oxide (GO), generated from graphite oxide, is a graphene surface which contains a range of reactive oxygen functional groups. These functional groups make GO a prime candidate for functionalization as well as greatly improving its colloidal suspension. It is expected that the introduction of a sufficiently functionalized, high surface area nanomaterial into conventional PEMs will improve ion conduction through more concentrated charge carrier species.

Graphene oxide (GO) was prepared by the improved hummer's method from graphitic flakes.[26,97,98] Graphite powder (2 g) is added to a 2 L round-bottom flask in an ice bath. Concentrated sulfuric acid (H_2SO_4 360 mL) and phosphoric acid (H_3PO_4 40 mL) is stirred

mechanically for 1 hour. Potassium permangonate ($KMNO_4^-$ 18 g) is added very slowly and the ice bath temperature is maintained below 4^oC. It is switched to a 50^oC oil bath for 16 hours, then put back to ice. Distilled and deionized water (DDI 400 mL) is added drop-wise to the solution, generating heat and gas. Hydrogen peroxide (H_2O_2 30 mL) is added drop-wise to the solution, observing a colour change to yellow as permanganate is completely neutralized. The graphene oxide is purified by washing in DDI, 30% v/v hydrochloric acid (HCl), a 50% v/v mixture of ethanol and DDI, 5% v/v HCl and a second time with DDI. The GO is suspended in DDI and stored in a sealed glass vial under ambient conditions.

To determine GO concentration a known volume is extracted and freezedried (Labconco Freezone1) at 0.08 mBar for at least 72 hours. The result is a highly porous and brown sponge-like material which is weighed to determine the solution concentration. When storing dried GO, great care is taken in preventing contact with any moisture.

3.1.2 Mesoporous Silicon Dioxide

A second high surface area nanomaterial is mesoporous silicon dioxide (SBA-15). Following established proecedures,[99,100] SBA-15 was prepared by combining a triblock copolymer P123 ($EO_{20}PO_{70}EO_{20}$, MW 5800, Aldrich Co., 2.2 g) in 2.0 M HCl (60 mL) until completely dissolved. Tetraethyl orthosilicate (TEOS 4.2 g) was added while vigorously stirring over a 10 minute period. The solution was left sitting for 24 hours at 40^oC in an autoclave, and a further 24 hours at 100^oC. The solution was washed with DDI and ethanol and dried overnight at 100^oC. A furnace (Thermo Scientific Lindberg Blue M) was used for calcination at 550^oC in air for 6 hours. The resulting white powder was analyzed using BET, SEM and XRD.

3.1.3 Sulfonic Acid Functionalization

An increase in sulfonic acid functionalization is essential to improve the number of active charge carrying species in a proton exchange membrane.[74,101] Integrating a sulfonated high surface area, hydrophilic nanomaterial is one method to increase SO_3H concentration. Sulfonic acid functionalization was performed on GO to form SA-GO, on SBA-15 to form SA-SBA, and also on various ratios of a mixture of the two nanomaterials at 33:66, 50:50 and 66:33 % w/w equivalent. From literature, mercaptasilane attacks exposed hydroxyl and epoxy groups to form new sulfonic groups onto the surface of the desired nanomaterial.[26,102] Graphene oxide functionalization (Figure 3.1) and silicon dioxide functionalization (Figure 3.2) are hypothesized to differ in two regards. GO has a significant number of epoxy and hydroxyl groups[103] which results in an increase in SO_3H functionalization. SBA-15 on the other hand is a mesoporous silica structure with a high surface area around 600-900 m^2 g^{-1}.[104,105] The inner pore walls are lined with hydroxyl species with which mercaptasilane functionalization can occur.[99] It is difficult to determine the degree of sulfonation (DS) from simple understanding of the structure, as dispersed graphene sheets in solution is favourable for functionalization while the high mesoporous surface area of SBA-15 could support additional SO_3H groups.

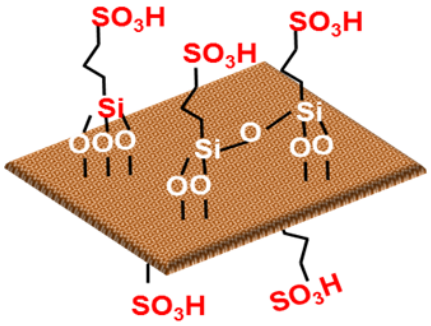

Figure 3.1: Sulfonic-acid doped graphene oxide (SA-GO)[106]

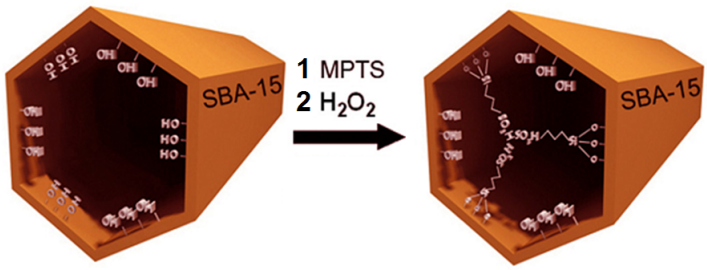

Figure 3.2: Proposed sulfonization mechanism in silicon dioxide pores to form SA-SBA

The desired high surface area reagent, for example GO (Fig. 3.3), is dispersed in Toluene for 4 hours. 3-mercaptopropyl-trimethoxysilane (MPTMS) at a 20:1 w/w % ratio

is added. Functionalization of thiol groups onto the dangling hydroxide bonds occurred in agitated solution at room temperature over 48 hours. A higher temperature would speed up this reaction, however it also has the potential to oxidize the nanomaterials of interest. The solution is centrifuged in ethanol, and the filtrant is tested with iodine (I_2 1 mg mL^{-1}) until MPTMS is no longer detected. The powder is left to air dry, and then stirred in 30% v/v H_2O_2 for 24 hours. It is washed with DDI and then redispersed into 0.5 M H2SO4 and for another 24 hours. To recover the dried, functionalized material, it is washed in DDI and freezedried (Labconco Freezone1) for at least 72 hours. Sulfonic-acid doped nanomaterials were given the abbreviation SA- to indicate functionalization.

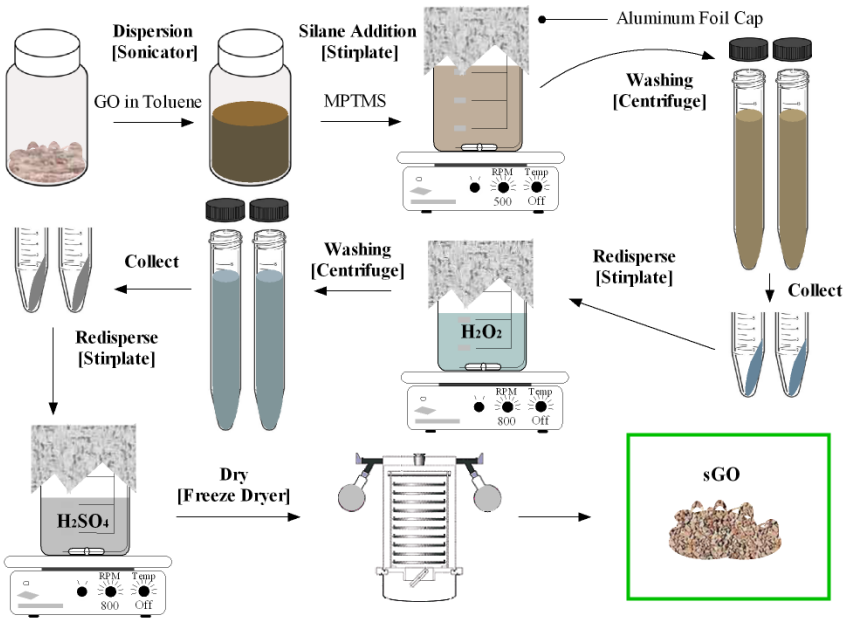

Figure 3.3: Simplified procedure for sulfonic functionalization of graphene oxide via silation of dangling hydroxyl species

3.2 Membrane Synthesis

3.2.1 Casting Trays

A solid-state polymer membrane is solution cast from a volatile organic solvent. Due to the requirement for perfectly level and large-scale membrane casting at elevated temperatures, several casting trays were fabricated for the project. 3D solidworks designs were proposed and accepted by a machine shop (Appendix A.1-A.4). The parts were machined by an automated computer numerical control (CNC) device (HAAS VF-2). Two variants at cast surface areas of 28.5 cm^2 and 38.4 cm^2 were used to form all the membranes presented.

3.2.2 Membrane Casting Conditions

Nafion ™Ionomer (15 wt%) was purchased from Ion Power Inc. To cast PFSA-based nano-composite membranes (Fig. 3.4), the solution was first cast at 80^{o}C for 12-24 hours and then redissolved into anhydrous N,N-dimethyl formamide (DMF) at 60^{o}C. Nanomaterials were suspended in DMF via sonication for 4 hr. The two solutions were mixed for another 4 hours, and then cast into a glass-bottom aluminum casting plate. The casting plate was left in an oven (Uamato DX 300) at 80^{o}C for 12 hours to form a solid membrane, then heated at 120^{o}C for 2 h, 160^{o}C for 1 h and 190^{o}C for 1 hour to evaporate any remaining DMF. All PFSA-based films were pre-treated by boiling (60^{o}C) in 3 wt% H_2O_2, rinsing 1 h in boiling DDI, boiled in 0.5M H_2SO_4 for 1 hr and again rinsed in DDI for 1 hr. PFSA-based membranes were left soaking in DDI until ready to be manufactured in an MEA.

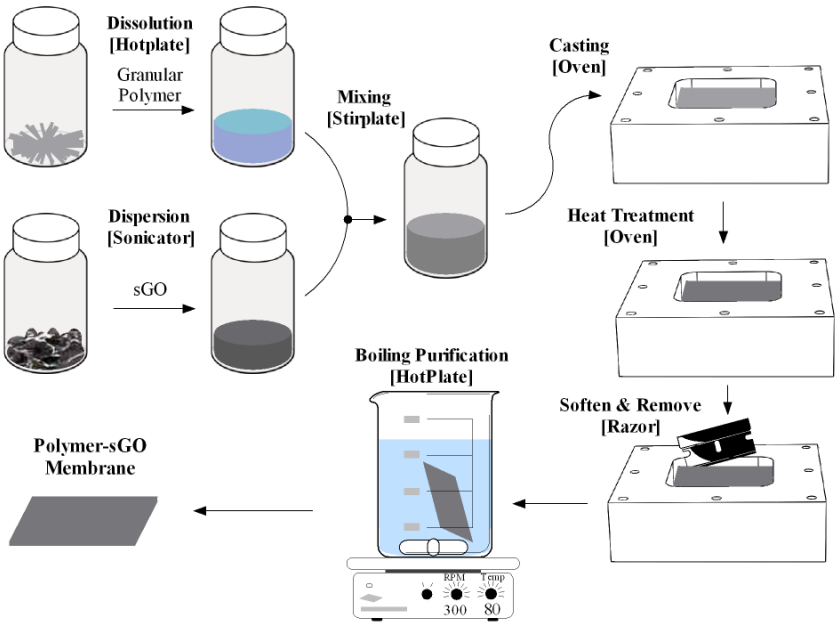

Figure 3.4: Simplified procedure for synthesis of a polymer SA-GO nanocomposite membranes

3.3 Characterization Techniques

3.3.1 FTIR

FTIR measurements were conducted on sodium chloride (NaCl) pellets. Nanomaterial powder was dispersed in ethanol, drop-cast onto the pellets and left to dry overnight in a glass desiccator chamber. The FTIR equipment (Bruker TENSOR 27) recorded a spectrum from 4000 to 500 cm^{-1}.

3.3.2 XRD

An x-ray diffractometer (XRD Rigaku MiniFlex600) was used to generate the x-ray spectrum from a copper target. Scans were performed from +3 to $+90^o$ 2θ degree from freeze-dried powder samples loaded onto a glass tray.

3.3.3 SEM and EDX

Scanning electron microscopy (SEM) and energy-dispersive x-ray spectroscopy (EDX) images of nanomaterial powder and cross-sectional membranes were performed using a LEO 1530 FESEM.

3.3.4 TEM

Transmission electron microscopy (TEM) images were obtained by sending samples to the McMaster Electron Microscopy Facility (JEOL 1200EX TEMSCAN).

3.3.5 BET

Brunauer-Emmett-Teller (BET Micromeritics ASAP 2020) was used to measure the specific surface area of powder nanomaterials.

3.3.6 Proton Conductivity

3.3.6.1 EIS

Electrochemical impedance spectroscopy (EIS) is a technique for differentiating losses based on measuring how a system impedes the flow of current. Unlike resistance, impedance deals with time or frequency dependencies. We know that resistance is the ratio between voltage and current, and we can define the impedance (Z) as

$$Z = \frac{V(t)}{i(t)} \tag{3.1}$$

Typical measurements are made by applying a sinusoidal voltage perturbation and monitoring the current response. This response may be shifted in phase compared to the

voltage perturbation, and is described by θ in complex notation

$$Z = \frac{V_o e^{jwt}}{i_o e^{jwt - j\theta}} = Z_o \cos\theta + Z_o \sin\theta j = Z_{real} + Z_{imaginary} \tag{3.2}$$

where Z_o is V_o/i_o and j is the imaginary number. A graphical representation of $-Z_{im}$ vs Z_{re} is known as a Nyquist plot, which summarizes impedance behaviour over many orders of magnitude in frequency.

The major contribution to ionic resistance in a FCS is the membrane. To simplify the analysis required, fuel cell sensors and MEA were not tested, instead opting to directly test the fabricated membrane. As the membrane acts as a simple resistor, the i-V curve is expected to be linear allowing for a relatively large perturbation. A potentiometer (Princeton VersaSTAT MC) is operated at a D.C. bias of 0.0 V vs OC, while the A.C. perturbation of 300 mV RMS is scanned from 1 MHz to 1 Hz at 30 points per decade. To determine the membrane resistance, linear extrapolation of the applicable high frequency response (HFR) on a Nyquist plot to the real impedance axis is accepted as the membrane ionic resistance.

3.3.6.2 Cross-plane Conductivity

To measure membrane cross-plane conductivity, a small teflon setup was fabricated with 4 platinum wires (Fig. 3.5). A membrane sample with dimensions of 0.5 mm by 2.0 mm is cut and placed onto this set-up, then torqued to 5 lbs by a torque wrench (FAT Wrench 5553556). The two outer platinum wires are connected to the counter and sensing electrode, while the two internal platinum wires are connected to the reference and second working electrode. Each electrode is spaced 3 mm apart, such that Eq. 3.3 becomes Eq. 3.4.

$$\sigma = \frac{L_{electrode-electrode}}{A\ R_{ionic}} \tag{3.3}$$

$$\sigma(\text{S cm}^{-1}) = \frac{0.3\text{ cm}}{T\ W\ R_{ionic}} \tag{3.4}$$

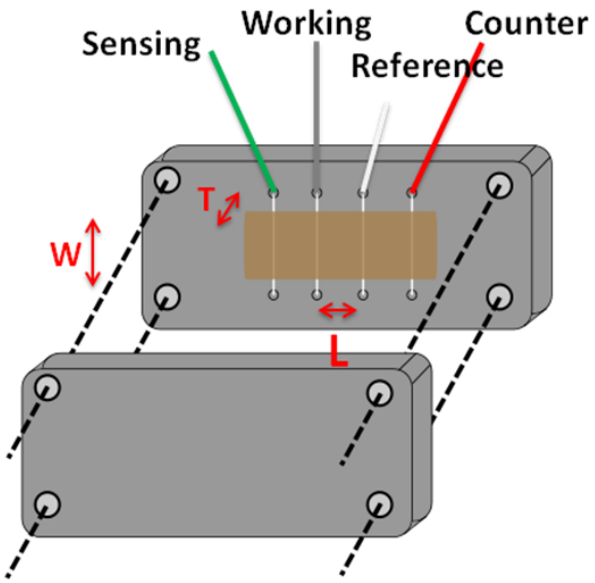

Figure 3.5: Cross-plane probe and membrane placement for ionic conductivity by EIS

In order to control membrane humidity during impedance testing an additional humidity chamber was fabricated. A sealed borosilicate glass dish was modified with rubber-stopped holes for conductive wire entry, temperature and humidity probes as well as a sealed connection to controllable humidified nitrogen (N_2) gas. This chamber is situated on top of a hot-plate for temperature control. Through use of a low N_2 flow rate, temperature variation between the inlet and outlet of the chamber was maintained below 2^oC, while humidity was measured as close as possible to the internal setup. For 100% RH tests, membranes were first soaked in DDI for at least 24 hours, then immediately tested for through-plane or cross-plane conductivity in ambient conditions.

3.3.6.3 Through-plane Conductivity

To measure through plane conductivity, a 3D printed design (Appendix A.5) was made which could be torqued to apply pressure to the membrane and ensure good contact. Overlapping platinum foil at 5 mm by 5 mm formed the conduction area as depicted in Figure 3.6. Several of these set-ups were made such that tests could occur in tandem.

Each cell was torqued to 10 lbs force before testing impedance. Samples were equilibrated in flowing N_2 for 24 [hr] to get the low humidity (25% RH) points, and equilibrated at least one hour for any other condition to ensure stability of the temperature and humidity levels.

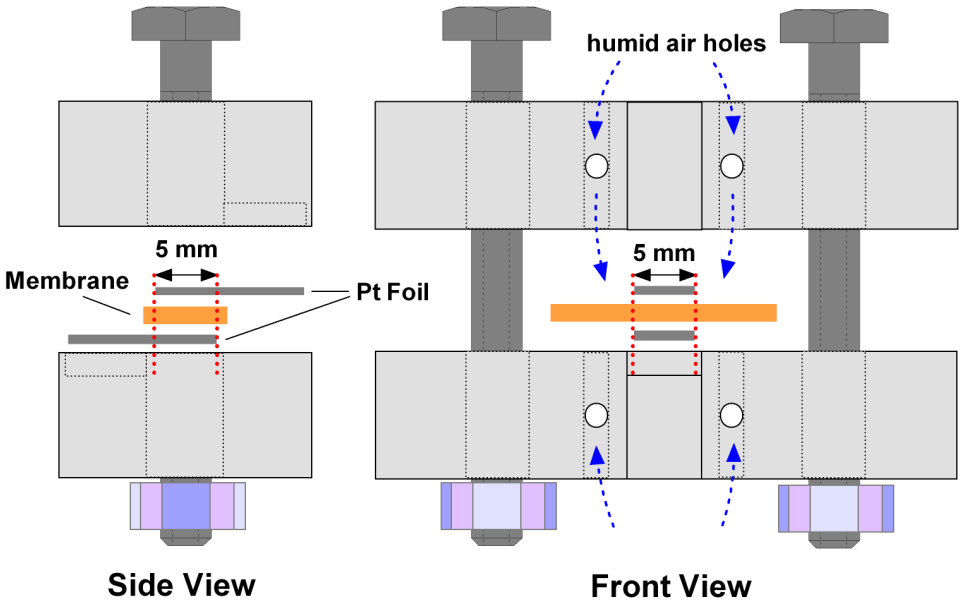

Figure 3.6: Through-plane schematic with improved humidity access and known cross-sectional area

3.3.7 Membrane Water Uptake

Water uptake (WU) measurements are integral to PFSA-based films. In order for high ionic conductivity and full dissociation of the integrated sulfonic acid groups, the presence of water is according to the equilibrium

$$-SO_3H + H_2O \longleftrightarrow -SO_3^- + H_3O^+ \tag{3.5}$$

Improved water uptake will indicate less sensitivity to the environment as more water

molecules need to be removed to change ionic conductivity. To measure, membranes are soaked in DDI for at least 24 hours, blotted dry with a KimTek wipe and sample weight is recorded. Thickness and width is measured with a micrometer (Mititoyo 293 MDC-MX Lite). Length is recorded with a caliper (Wixey WR100) and weight is recorded by a high accuracy balance (d = 0.01/0.1 mg Denver Instrument MXX-2001). The membrane is dried in a vacuum oven (VWR 1410) at 60^{o}C and 30 mmHg for 24 hours before the dry weight is recorded. Each weight is repeated 5 times, with a 5 minute break between weighing. The WU and swelling ratio (SWR) is calculated by

$$WU(\%) = \frac{w_{wet} - w_{dry}}{w_{dry}} * 100 \tag{3.6}$$

$$SWR(\%) = \frac{V_{wet} - V_{dry}}{V_{dry}} * 100 \tag{3.7}$$

where w is the weight recorded and V is the membrane volume equal to the multiplied average of each width, length and thickness.

3.3.8 IEC and Mobility

Ion exchange content (IEC) sometimes also called ionic exchange capacity or degree of sulfonation (DS) expresses the content of sulfonic acid groups in mmol g^{-1}. It is known that the water solubility of a polymer electrolyte increases with IEC, typically at the expense of mechanical strength and correlated with an increase in water uptake.[107] IEC was performed using a 25 mL titration pipette. Membrane samples (approximately 20 mm by 20 mm) were first immersed in DDI for 24 hours and the weight recorded. These were soaked in 0.1 M sodium chloride (NaCl 50 mL) solution for 24 hours in ambient conditions. The membranes are removed and dried for 24 hours at 60^{o}C in a vacuum oven (VWR 1410) at 30 mmHg. 0.01 M sodium hydroxide (NaOH) was used as a titrant against the remaining solution until a pH of 7.0 is observed using a phenolphthalein indicator. The IEC and

equivalent weight (EW) is calculated from

$$IEC = \frac{V_{NaOH} * c_{NaOH}}{w_{dry}} = \frac{SO_3H\ group}{g_{polymer}} = \frac{1}{EW} \tag{3.8}$$

From the calculation of IEC and knowledge of the WU of the same membrane, the water content (λ) can be calculated by

$$\lambda = EW * \frac{w_{wet} - w_{dry}}{M_{H_2O} * w_{dry}} = \frac{\text{mol}\ (H_2O)}{SO_3Hgroup} \tag{3.9}$$

where M_{H_2O} is the molar weight of water.

Further, the proton mobility can be calculated by

$$\text{u}(\text{H}^+) = \frac{\sigma\ WU}{F\ IEC} \tag{3.10}$$

where F is Faraday's constant and σ is the through-plane conductivity. Through analysis of the proton mobility, we can assess the impact of morphological changes with a fixed sulfonic acid content. By integrating specific nanomaterials, the proton pathway will be enhanced or inhibited depending on the spacing and ease-of-access to the sulfonic proton transfer groups. As we claim to enhance conductivity through a morphological shift rather than from increases in sulfonic acid concentration, the proton mobility becomes a key indicator.

3.4 Alcohol Fuel Cell Sensor Testing

3.4.1 MEA Fabrication

The PFSA-based membrane was constructed into a membrane electrode assembly (MEA) using a hot-press machine (Carver 3912). Platinum coated carbon paper (0.5 mg/cm2 CP-80 from FuelCellsEtc) was used as both the anode and cathode electrodes.

These were directly hot-pressed to the polymer membrane without the need for any binding agent at 0.2 Ton force, 135^{o}C for 3 minutes and were very mechanically robust. A 16 mm (diameter) punch die (MTI MSK-T10) was used to evenly cut the MEA to fit into a housing.

3.4.2 MEA Equilibration and Sensor Construct

Plastic housing (Fig. 3.7) was acquired to store and test the fabricated MEAs. Each housing had two exposed platinum wires, sealed with Elecolit 4030 conductive epoxy. Small plastic fins within the cell served a dual purpose in creating a fuel 'channel' from inlet-to-outlet, while also supporting the cylindrical MEA and ensuring good contact between the platinum wire and each electrode surface.

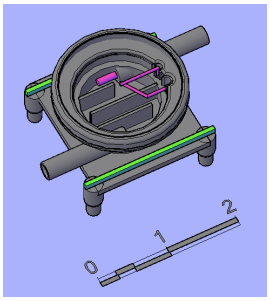

Figure 3.7: Plastic housing model where purple indicates metallic components, scale is in centimeters.

Prior to full cell testing, the 16 mm fabricated MEAs were equilibrated for 24 hours in a humidity chamber (ASPEC BTL-433) at a constant 25^{o}C and 60% relative humidity (RH). These were then assembled into the plastic housing containers. A porous PVC spacer (1 mm thick, 16 mm diameter) was included on top of the cathode side to mimic the pressure in a commercial cell upon sealing with the plastic cap and ensure good contact with the platinum current collectors. This assembly was further equilibrated at least 48 hours before initial testing.

3.4.3 Full Cell Test Set-up

3.4.3.1 Simulator

A breath simulator is employed in order to produce the hundreds or even thousands of human-breath samples required to understand the effect of varied material parameters. Traditionally the simplest method to achieve this is to obtain a glass jar, dissolve ethanol into water at a known concentration into it and bubble air through that solution to a nearby testing station.[108] In order to maintain accuracy, the solution is continuously mixed as well as maintained at 34^{o}C, matching that of a typical human breath sample,[16,109,110] although this approximated value is contested by some.[108] In testing, a 500 mL Guth Laboratories Breath Simulator (Model 12V500) was used to maintain the ethanol analyte.

A 4 v/v % stock solution was prepared in the following manner: a 20 mL volumetric pipette was first rinsed 3x with distilled water (DI), and then 3 times with pure ethanol solution (99.9% purity). A 500 mL volumetric flask was rinsed 3x with DI, filled with DI to approximately 400 mL and 20 mL of ethanol is added. This solution was mixed and left to sit for 10 minutes to allow for temperature or volume disequilibrium. The volumetric flask was then filled and upended at least 15 times. A further 10 minutes for equilibration was given before use. The stock solution was remade whenever it ran below 100 mL or 1 month had passed, whichever occurred first.

To prepare a sample at 0.05 BAC (g dL^{-}1) a 1:50 dilution of 4 v/v % stock ethanol solution was mixed with distilled water using the same technique excepting a 10 mL pipette. Other BAC dilutions were performed using the same technique but varying the amount of stock solution transferred and the size of the transfer pipette. The resulting vapour concentration was verified with the ACS SAF'IR™EVOLUTION, a dual IR and fuel cell evidential breathalyzer. The value was compared to standard solutions provided by ACS at 0.05 and 0.10 BAC and found to be comparable and reliable.

It is well known that vapour emitting from a water and ethanol solution will result in a loss of ethanol due to its higher volatility and partial vapour pressure.[111] Most breath

simulators recommend replacement of the ethanol fluid after 50 uses, or 100 uses if in tandem.[112] For the purpose of testing the alcohol-water solution was replaced if left standing for more than 3 hours or after 30 uses, whichever came first. To combat the loss of ethanol, a recirculation system was proposed and developed where air would be drawn from the simulator instead of from the ambient environment. In practice this increased the pressure of the total system, causing ethanol molecules in the air stream to be pushed into the fuel cell sensor by diffusion before the sampling pump drew its allocated air sample and providing an erroneous and early response. As such, ambient air was drawn from the lab environment (24^{o}C, 40 RH) and heated as it is bubbled through the solution for all tests conducted.

3.4.3.2 Auto-sampling

The initial testing set-up was a stripped down Alcochek FC90 where the exposed sample pump was redirected from the fuel cell in the device to our external one. A sensor in the FC90 would detect an adequate flow rate equal to a human breath sample of 10 to 12 litres per minute and then the circuit would fire a 0.3 mL sampling pump after waiting for 3 seconds. The pump action would push stagnant air out of the cell into the breath stream and then draw in the analyte. A high accuracy 29 Ω resistor was placed in series with the fuel cell sensor and 6 1/2 digit digital multi-meter (Agilent 34411A) through a breadboard to reduce current fluctuation due to contact resistance. There were a significant number of issues with this set-up including fluctuating pump power, inconsistent detection of flow rate, varying total resistance and human error in sampling due to manual interaction.

A new high power solenoid pump was proposed which sampled a volume of 0.5 mL. The wattage required was determined using a QuadTech programmable DC power supply (Model 42006-100-25) and found to be 24 Watts. The data recording method is presented in Figure 3.8. In an effort to improve the accuracy and reliability of test data as well as reduce manual interaction, the breath simulation, breath sample and data collection must be linked and able to be computer controlled. Towards this end an integrated circuit (IC)

approach was employed where a fundamental electronic circuit is hard-wired to accomplish the control of these components and can be activated from a computer station.

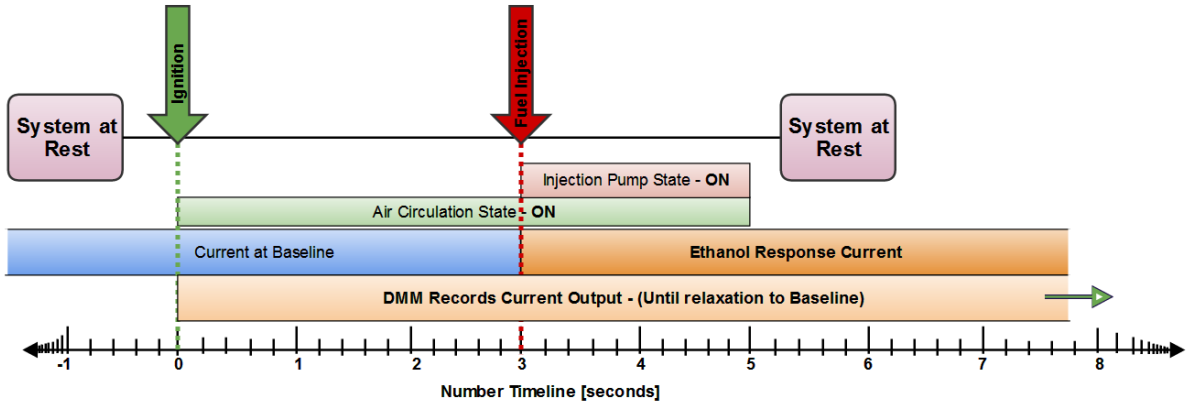

Figure 3.8: Fuel cell sensor data capture timeline

For our designed system we required two features. First, we needed an ON signal that lasts for the duration of the air pump. Second, we needed an ON signal that starts exactly three seconds after the first and that lasts for exactly two seconds. An NE555 IC acts as a timer, either starting in the OFF phase and turning ON after a specified time, or starting in the ON phase and turning OFF. The timing is controlled by the combination of a capacitor C and resistor R as described in Equation 3.1.

$$t(\text{sec}) = \ln(3) * C * R \ = 1.1 * C * R \tag{3.11}$$

It is simple to design an NE555 to turn ON for five seconds and control the air pump. If a second NE555 timer starting in the OFF phase is directly tied to the output of the first timer, it can be set to turn ON after three seconds and will lose power when the initial timer turns OFF. Unfortunately, these components have limited current passage, permitting a maximum of 0.2 A. As both the air pump and sampling pump require significantly more current at 1.9 and 6.7 A respectively with 12 V DC adapters, isolated high-amperage power

Table 3.1: Comparison of air pump model specifications

Air Pump Model Unit	**Flow Rate** lpm	**Size** mm	**Power** V	**Humidity** % RH	**Cost** USD
Parker D736A-23-02	11	85x76x33	24	N/A	288.00
Z712-6025-3800	$\leq$ 15	66x86x116	12/24	0-100	63.26
DX524-803-4800	16	102x70x40	12/24	0-100	51.26
Clark Boxer 3112	12	110x100x40	12/24	0-100	192.4

sources needed to be interfaced to the timer circuit using metal oxide semiconductor field effect transistors (MOSFETs) as electronic switches. Some additional components such as a manual ignition switch, LED indicator lights and diodes to prevent current backflow from capacitors and motors were necessary to complete the circuit design (Appendix A.6).

Several models of air flow pump were investigated (Table 3.1) and a 12 V humidity insensitive pump (Boxer 3112) operating at a flow rate of 12 litres per minute was purchased from Clark Solutions. A cheap environmental controller was purchased (Arduino R3) which translates command line input from a computer into hardware signals. This signal was hooked in parallel with the manual switch so that command line code could instantiate the electronic setup for a test run (Appendix C.1). A simple program was designed to interface with the data collection software from Agilent and simultaneously control the newly developed hardware (Appendix C.2). The parameters available to the user are the sample name, number of tests to run and duration of each test in seconds, defaulting to 10 and 180 respectively. Upon instantiation, the data recording tool and hardware would simultaneously start, the hardware would sample after 3 seconds and turn off at 5. Data collection will elapse for the specified duration, save the sample run using the sample name parameter with an automatic counter, and then restart both hardware and data collection until the number of runs is completed. All components, manufacturing and testing was assembled by hand for a total cost less than 400 CAD (Table B.1).

3.4.3.3 Data Acquisition

In industry methods are applied to simplify data analysis, namely the calculation of the response integral. As the ethanol current response relaxes towards the baseline, the reliable decay shape indicates that approximation can be made by choosing points along the relaxation curve to calculate the total integral (Eq. 3.6). This approximation is valid for conventional commercial sensors, however there was high variance in sample-to-sample runs using the same method with newly created membranes that show new response curve shapes. As the integral value depends significantly on the baseline or zero-current response, slight fluctuations in the baseline value or over-run of a previous test would throw off the value of $Area_{true}$.

$$Area_{true} = Area_{\frac{3}{4}Peak} + 2 * (Area_{\frac{3}{8}Peak} - Area_{\frac{3}{4}Peak}) \tag{3.12}$$

A new method was proposed to use a fitting function to forward extrapolate a segment of the well-ordered decay. It turns out that the decay of ethanol current response is best fit by a logistic model (Eq. 3.7). This model is used in dose-response systems for drugs. We can consider ethanol to be the "dose" and the current output as the "response" to find a quick and accurate fit (Adj. $R^2 = 1.0$) even when specifying the error tolerance as $\epsilon = 1e^{-}6$. Using this fitting, a very accurate baseline can be calculated and integrated from. Upon applying this methodology to the data-sets already analyzed with the prior method (Eq. 3.6) the peak area standard deviation decreased significantly.

$$y = \frac{A_1 - A_2}{1 + (x/x_o)^p} + A_2 \tag{3.13}$$

The logistic model is easily computed by laboratory software (OriginPro 8.5 SR1), and so a script was written in C to automatically import, format, fit and integrate the raw data curves (Appendix C.3). Some additional coding was also performed to detect and ignore data points related to humidity. For Nafion ™based samples with very low humidity

conditions, when they first come into contact with a humid source there is an initial 'burst' of current flow which quickly resolves. By using OriginPro coding to detect this initial peak, detect if it is significant and then repress the data before taking the integral a great deal of effort in manual analysis was avoided.

3.4.3.4 Accelerated Degradation Testing

The goal of degradation testing is to stress the environment of the cell and evaluate how it reacts. The basic premise is that any degradation test is valid as long as it is applied consistently. If any procedure is repeated reliably it is considered valid for comparison to other samples in similar conditions. Due to the variety of membrane characteristics including thickness, composition level and additives at investigation, a simple degradation method was chosen (Fig. 3.9) which is listed more completely in Table B.2. This simplified procedure is able to handle several samples per day in our test environment while still enforcing a harsh environment. The time required for a single sample on a given day is a total of 3.5 hours. With only one automated testing station, the samples must be staged by at least 30 minute intervals. A typical test would run during a work week (5 days) where a baking cycle (2 hours at 60^{o}C, VWR 1300U Oven) is run once per day, involving between 4 to 6 samples.

3.4.3.5 FCS Reliability

The sensitivity of a sensor is calculated from the slope of a concentration versus full cell response. To collect this data, a range of alcohol solutions from 0 to 200 mg dL$^-$1 (equivalent to 0 to 0.200 BAC) are created. The integral of the response is recorded as the number of electrons participating in the reaction. A high slope of the linear fit indicates a sample with improved sensitivity. The sample accuracy is shown by the LOF of the linear model, with samples showing a 0.99 or higher Adj. R^2 demonstrating meaningful.

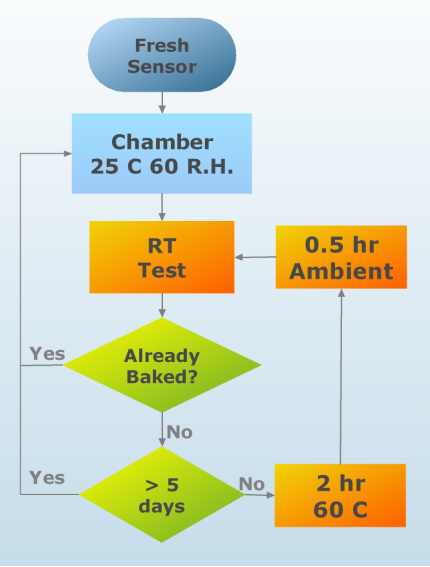

Figure 3.9: Degradation test method for fuel cell sensors during full cell testing

Chapter 4

Results and Discussions

4.1 Commercial Membranes

4.1.1 H_2SO_4 soaked PVC

The standard degradation cycle was applied to a 2-year old commercial sensor in the full cell test environment before taking it apart for characterization. The response appeared to be both reliable and environmentally stable (Figure 4.1), showing a consistent peak area even after four subsequent exposures to a high temperature environment. The other important parameters, namely the peak height, response time (time-to-peak) and recovery time all showed a stable response. Although not shown in the Peak Area, the standard deviation for each data point was calculated and shown to be lower than 2% of the total value (Table 4.1). This sample, although a pseudo-liquid electrolyte, is important as it defines the benchmark for commercial viability.

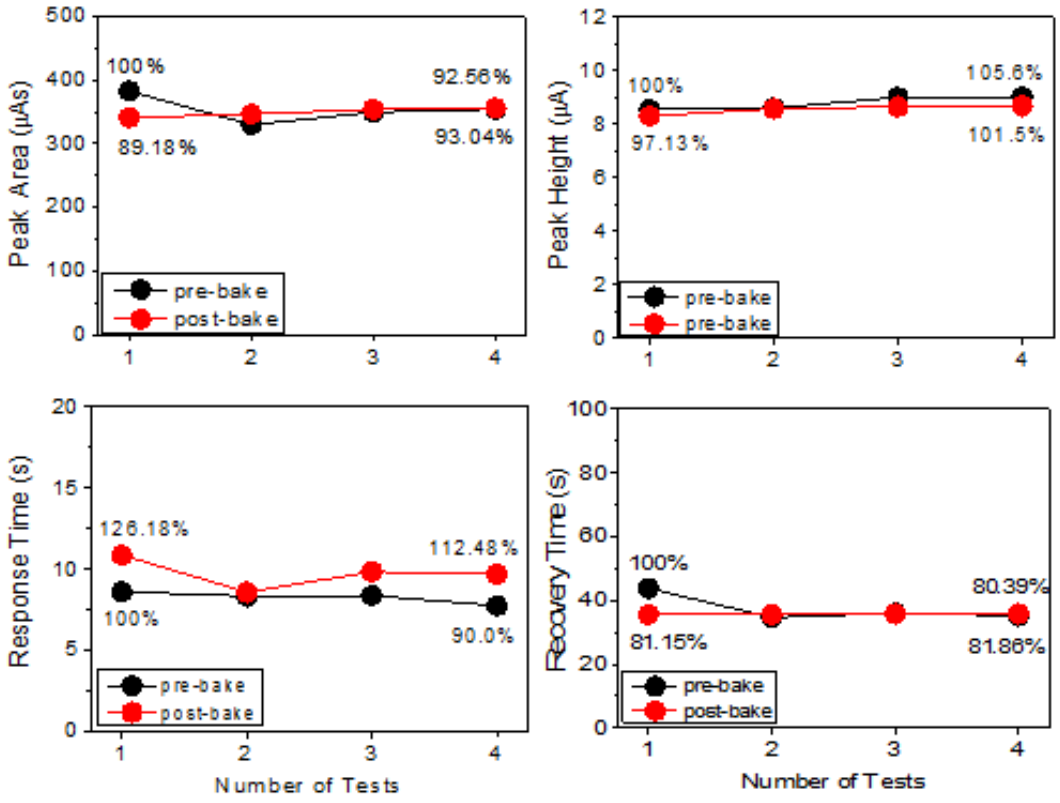

Figure 4.1: Summary of the degradation results for a 2 year old commercial sensor recovered from an evidential breathalyzer. Pre-bake is a response after at humidification in a 25^{o}C, 60 RH chamber, post-bake is a response after degradation exposure at 60^{o}C.

4.1.2 Nafion

To compare samples to modern Nafion ™as a baseline, several full cells were fabricated from commercial membranes and the PFSA ionomer. Nafion 115 ™(127 µm) and 117 (183 µm) membranes were prepared by membrane cleaning in boiling water, hydrogen peroxide and 0.5 M hydrochloric acid as described previously. Re-cast membranes at 100 µm and 220 were µm were first cast from commercial solution, then recast in DMF and cleaned. For simplicity, the raw data curves are shown comparing initial testing after standard humidification at 25^{o}C and 60 RH versus 20 hours of humidification following a single 2 hour 60^{o}C degradation test. From the results (Figure 4.2) it is clear that several factors are affecting the fuel cell sensor response.

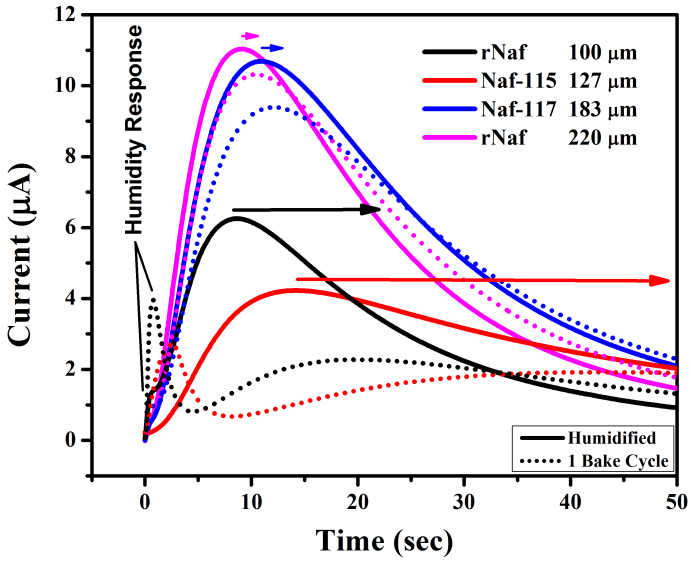

Figure 4.2: Selected response curves from a sensor response constructed with commercial Nafion ™

Low thickness is theorized to provide a poor response due to increased ethanol cross-over.[47] A humidity peak is observed for thin samples, where the introduction of humid air

creates a sudden proton and current flux. The thicker membranes suffer less in terms of response height and time-to-peak change (shown by the arrows in Figure 4.2). Extrapolating this result we could claim that a reliable response would be possible with very thick Nafion ™films, say 600-1000 µm. However, the material cost to prepare such a thick film while still theoretical observing water loss makes it commercially infeasible compared to acid-soaked membrane alternatives.

The reliability of the membranes is evaluated based on two criteria: degradation standard deviation and testing standard deviation. These both contribute to a source of error in the response. The former is the long-term response change (requirement for calibration) and the latter is the short term response change (reliability of repeated tests). Table 4.1 lists the figures for thick Nafion™-based sensors over a degradation testing cycle of 4 days (8 tests with 5 responses each).

Table 4.1: Peak Area Sensitivity for commercial Nafion membranes

Sample	**Thickness**	**Avg. Peak Area**	**St. Dev.**	**Max St. Dev. within tests**
Units	µm	µm s	%	%
Naf-115	127	295.10	14.90	5.38
Naf-117	183	394.43	5.62	2.58
rNaf	220	350.91	3.85	4.43
Acid-Soaked	1100	500.78	1.70	1.69

Clearly, thick Nafion ™membranes exhibited an ethanol FCS response which was both strong and reliable. Yet to attain the same performance as acid-soaked polymer electrolytes there needs to be additional improvements. One proposal is the introduction of functionalized nanomaterials to increase the sulfonic acid content.

4.2 PFSA-SA-GO Composite Membrane

The solid polymer membrane composited with sulfonic acid graphene oxide (SA-GO) had been previously investigated as a solid-state electrolyte in hydrogen fuel cells.[26] Significantly improved membrane performance at low humidities (4 times higher than recast PFSA) is attributed to a higher water uptake. This phenomena was tested for the FCS by manufacturing SA-GO nano-composite membranes with varied thickness between 200-400 µm and content percentiles from 3-10 wt%. Composite membranes at 10 wt% were unable to survive the cleansing process in boiling H_2O_2, showing internal gas generation and water uptake. Successful films at 7 wt% were realized by lowering the cleaning temperature to below 70^oC. The peak area response and deviation is listed in Table 4.2 while other material factors are graphically presented in Figure 4.3.

Table 4.2: Peak area sensitivity for PFSA SA-GO membranes with varying thicknesses and compositions

Sample	**Thickness**	**Avg. Peak Area**	**St. Dev.**	**Max St. Dev. within tests**
Units	µm	µm s	%	%
3% Naf-SA-GO	230	336.57	4.3	7.33
3% Naf-SA-GO	350	347.07	4.13	5.21
5% Naf-SA-GO	240	379.25	2.41	4.34
6% Naf-SA-GO	360	447.13	3.24	2.33
7% Naf-SA-GO	215	335.25	1.88	9.58

From these results, we find some non-linear behavior in membrane performance. The best sample considering only alcohol detection, meaning peak area response, is the 6 wt% SA-GO in PFSA due to low inter-test deviation, reasonable decay during degradation testing and an improved current area response. However from a commercial or consumer stand-point, the 5 wt% sample displays similar stability but improved response times (Fig. 4.3). Further, by comparing the results of varied thicknesses, ie 3 wt% 230 µm versus 350 µm and comparing both 5 wt% and 7 wt% versus the thicker 6 wt%, it seems that drastically

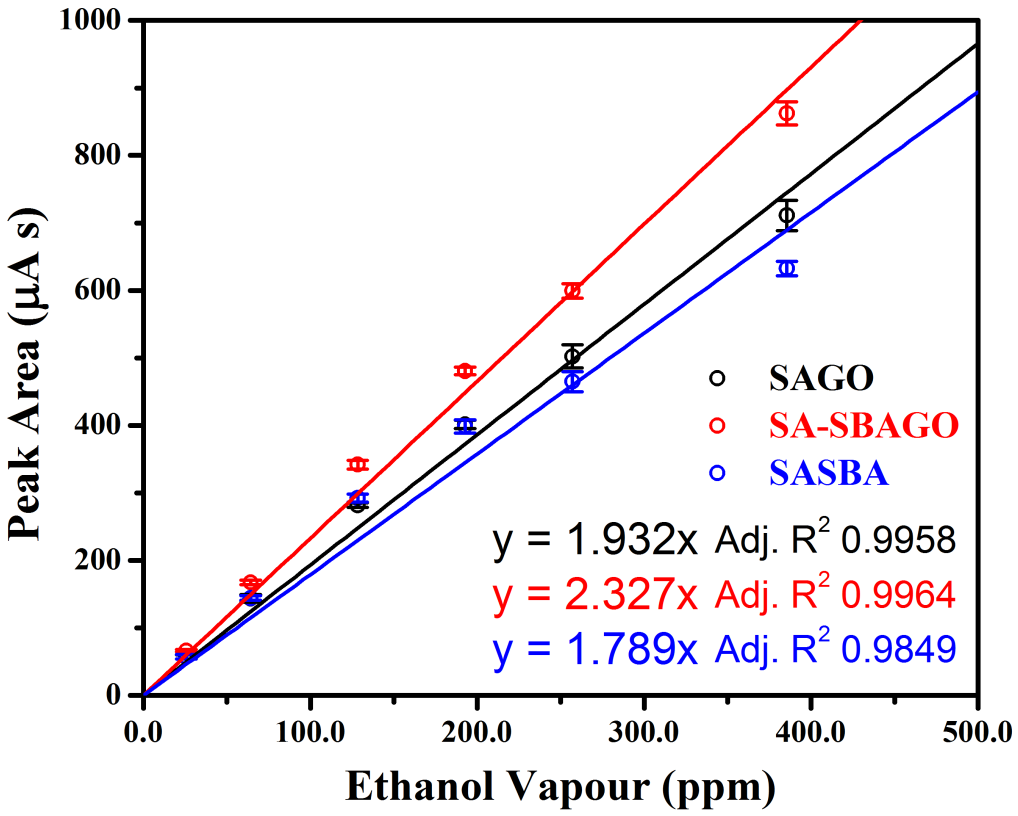

Figure 4.3: Selected response curves from a sensor response at different membrane thicknesses

increasing the membrane thickness is no longer providing significant improvement to the sensor response. The added cost of ionomer solution outweights the marginal gains provided as the thickness increases. The increased performance is not on the same scale as evidenced when moving from thin ($\leq 150\mu m$) membranes, thereby demonstrating a non-linear trend.

The response curve at the same thickness as raw PFSA is smaller (Fig. 4.4) yet shows remarkable stability. Commercial Nafion ™membranes showed significant response change after only a single exposure to the accelerated degradation environment as shown previously in Figure 4.2. Membranes prepared with SA-GO content have very little change even after four degredation exposures, demonstrating higher reliability. Judging solely from their response curves it appears that the 3% SA-GO has drastically reduced the initial performance; Figure 4.4 [Right] demonstrates how the current area is provided by the so-called *tailing* effect. As the platinum catalyst is not rate limited by the small amount of fuel present, the mass transfer or ionic conductance of protons is the proposed factor to be limiting the response rapidity. Thus it appears that the addition of even a small percentile of SA-GO is impeding the flow of protons while retaining and improving the water uptake. Increasing SA-GO content to 5 wt% and further to 7 wt% both demonstrate improved response times, implying that a morphological change may be occurring to permit flow.

It was hypothesized that at low wt%, the functionalized GO sheets align horizontally during solution casting. Increasing the wt% content begins to disrupt this alignment, eventually becoming so convoluted that it forms void volumes where gas and water is trapped internally and ruptures the film in order to escape. Due to the preparation stability and reasonable response of the 5 wt% SA-GO membrane, future membranes were all cast with 5 wt% nano-material content for comparison.

4.3 PFSA-SA-(SBA:GO) Composite Membrane

There is support in literature for the restacking of sulfonated GO and its tendency towards a layered structure in a polymer matrix.[28,113] A more recent study on sulfonated

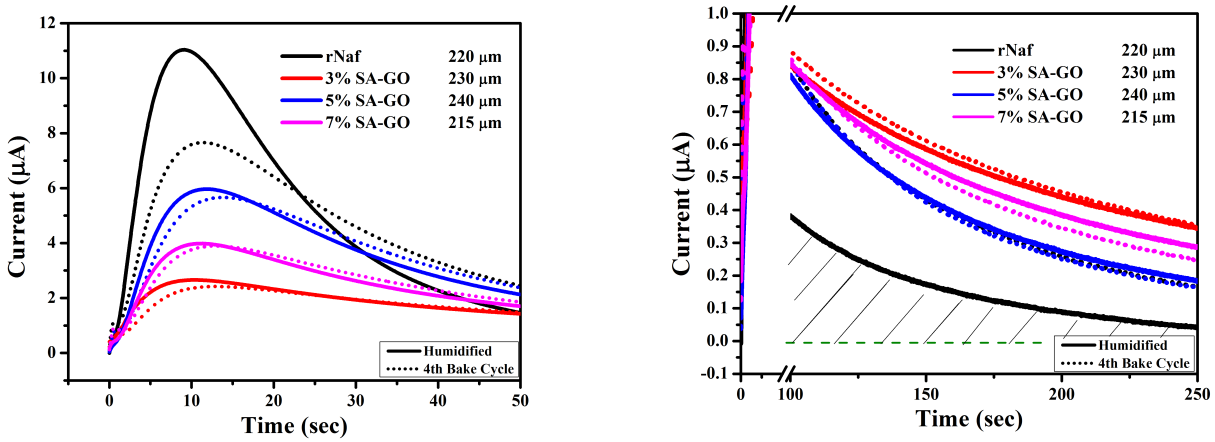

Figure 4.4: Degraded response curves comparing wt% SA-GO and pure PFSA membranes [Left] Peak height and decay over 4 bake cycles [Right] Expanded view of tailing effect to demonstrate similar peak area responses

GO-SiO_2 claimed to observe aggregation above 0.8 wt% and positively affect the solid state polymer membrane's structural maintenance by suppressing polymer chain movement.[114] To investigate this theory that the consistency of the GO layers can be broken up by inserting non-sheet-like nanoparticles (Fig. 4.5), mesoporous silica (SBA-15) was introduced. SBA-15 has literature support in post-synthesis functionalization of sulfonic groups, a large surface area and a cubic structure making it a prime candidate for nanomaterial insertion.[99] In this way, rather than contributing excess SA-GO to enhance proton conduction, sheet stacking and alignment can be disrupted by a functionalized silica, both aiding in proton transport and the degree of sulfonation.

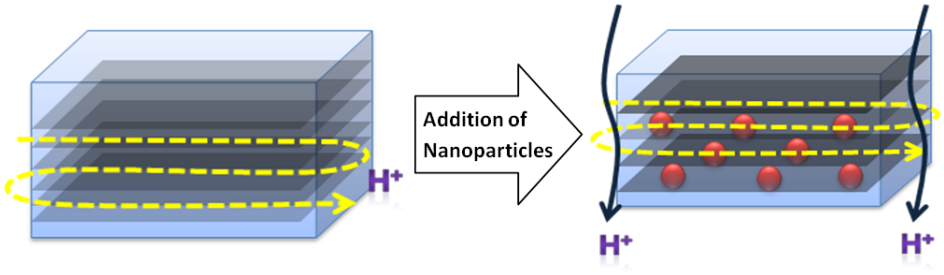

Figure 4.5: Schematic proposing integration of SBA-15 to improve through-plane conduction

Initially, three membranes were cast at 5 wt% nano-filler content. In the first, 5% SA-GO was present. In the second, a 50:50 w/w mixture of SA-GO and SBA-15. In the third case, a 50:50 w/w mixture of GO and SBA-15 was co-functionalized with MPTMS and tested. It should be noted that due to centrifugation and purification during synthesis, some deviation to the co-functionalized 50:50 w/w mixture is possible in the product. These membranes were subjected to the standard degradation testing cycle (Fig. 4.6). A very poignant observation is that the 2.5 wt% SA-GO and 2.5 wt% SBA-15 demonstrated an improved response curve compared to 5 wt% SA-GO; a drastic change compared to 3 wt% with a higher peak area, faster response curve and much improved recovery time at lower sulfonation. Upon co-functionalization, increasing the number of sulfonic acid groups present for ionic conduction while still breaking up the regularity of the 2.5 wt% SA-GO sheets even higher performance was observed.

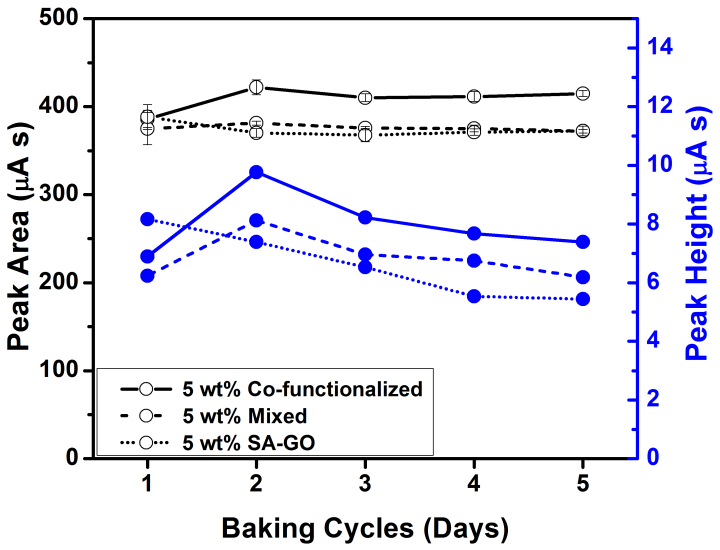

Figure 4.6: Peak area and height comparison between SA-GO and intercalated nanoparticle membranes

4.3.1 Co-functionalized Nanofiller

Previous investigation of the FTIR and XPS spectra comparing bulk GO to SA-GO[26,102] found that epoxy and hydroxyl vibrations (862 cm^{-1} and 1054 cm^{-1}) disappear after functionalization with MPTMS. The silane moiety hydrolyzes into silanols ($Si(OH)_3$) and is partially oligomerized in a condensation reaction. The silanol group and oligomers become coupled with epoxy and hydroxyl groups on GO during water removal. Oxidation of thiols will occur in the presence of H_2O_2 to form sulfonic acid surface species on GO (Fig. 4.7). FTIR investigation on SBA-15 compared to SA-SBA found the appearance of the C-H (2935 cm^{-1}) vibration as well as a weak -SH group (2580 cm^{-1})[99] and two SO_3H indicators (1060 and 650 cm^{-1}).[100]

The FTIR spectra of the novel co-functionalization is presented (Fig. 4.8). The strong presence of the C=O bond (1725 cm^{-1}) at 1:1 (SBA-15:GO) during synthesis indicates that sufficient SA-GO remained in the nanomaterial powder mix, alleviating previous concerns about precipitation during centrifugation. The Si-O vibrations for stretching, bending and rocking are obvious at 1100, 950 and 805 cm^{-1} respectively. Some SO_3H peaks are noticeable and correspond to literature.[100,102] This FTIR spectra confirms the functionalization of sulfonic groups as well as the presence of SA-GO and SA-SBA in the co-functionalized powder.

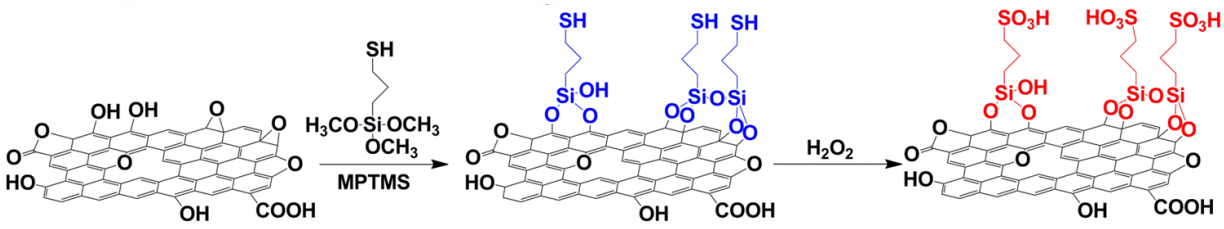

Figure 4.7: Proposed sulfonization mechanism on graphene oxide[102]

XRD of the SA-GO and SBA-15 ratios, including raw graphene oxide, are shown in Figure 4.9. The graphene oxide peak at 9^o is slighly lower than literature using the Improved Hummer's method[115] around approximately 10^o. Bulk graphite oxide obtained by

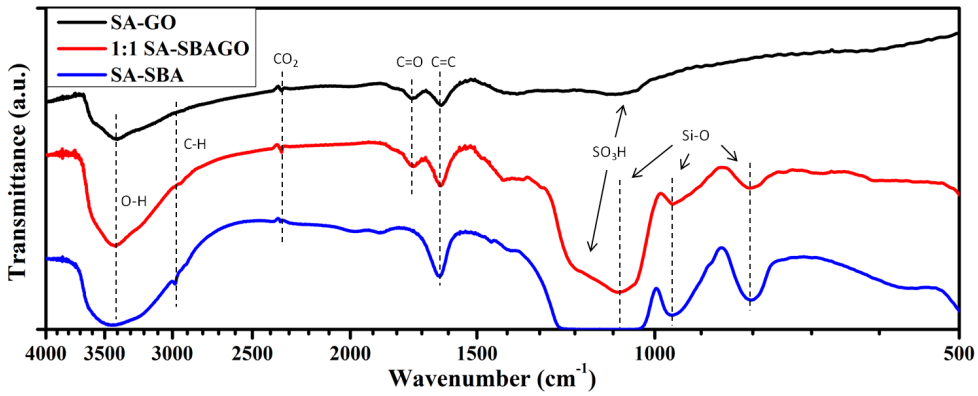

Figure 4.8: FTIR spectra of SA-GO and 1:1 SA-SBAGO

typical oxidation and purification results in a well defined peak at 11.0^o 2θ and constitutes the restacking of previously exfoliated single layer GO flakes. The observed low angle peak is strong, suggesting long-ranged order. If the ordered stacking of graphene layers is preserved and highly oxidized, forming a crystalline structure, this peak can be explained by a c-axis expansion on the original graphite flakes.[116] Sulfonic functionalization shifts the XRD peak to 10.3^o indicating exfoliation of the synthesized GO into single sheets during the functionalization step. This peak diminishes as expected when the SA-GO content ratio is lowered until only SA-SBA-15 is present. SBA-15 shows strong peaks in the 0.5-4^o 2θ region[117] which wasn't captured by our device operating from a starting angle of 3^o, but can still be observed by the tail end of a peak captured from 3^o to 7^o 2θ which is only observed in samples containing SBA-15.

After synthesis of SBA-15, BET analysis confirmed that a high surface area nanomaterial based on the polymeric template was formed. SBA-15 synthesized in neutral media will form disordered mesoporous silicas with uniform pores as large as 30 nm and cubic structures.[117] The measured average pore diameter (4 V/A) was 6.8484 nm (Fig. 4.10) with an average particle size of 4.9139 nm. BJH Adsorption showed a remarkable surface area measurement at approximately 700 m^2 g^{-1}, certainly large enough to provide significant sulfonic group functionalization.

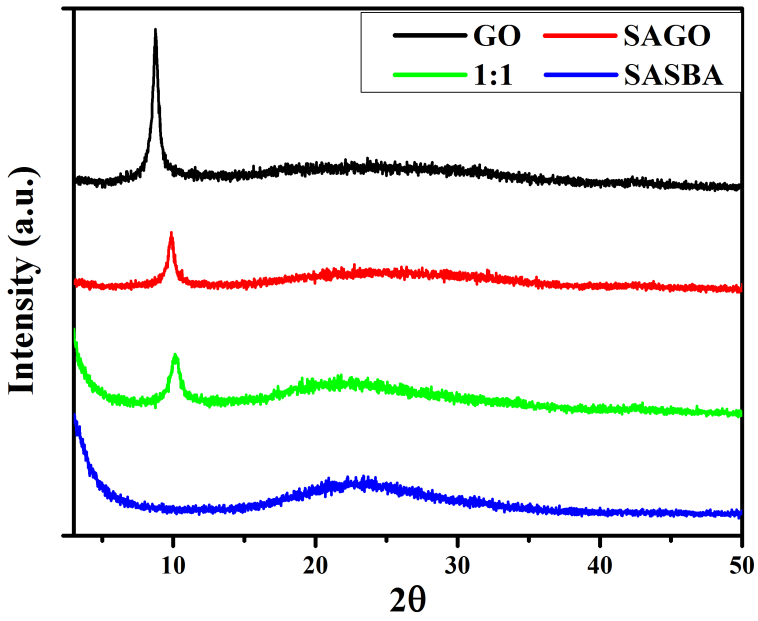

Figure 4.9: XRD of SA-GO and SA-SBA-15 powders

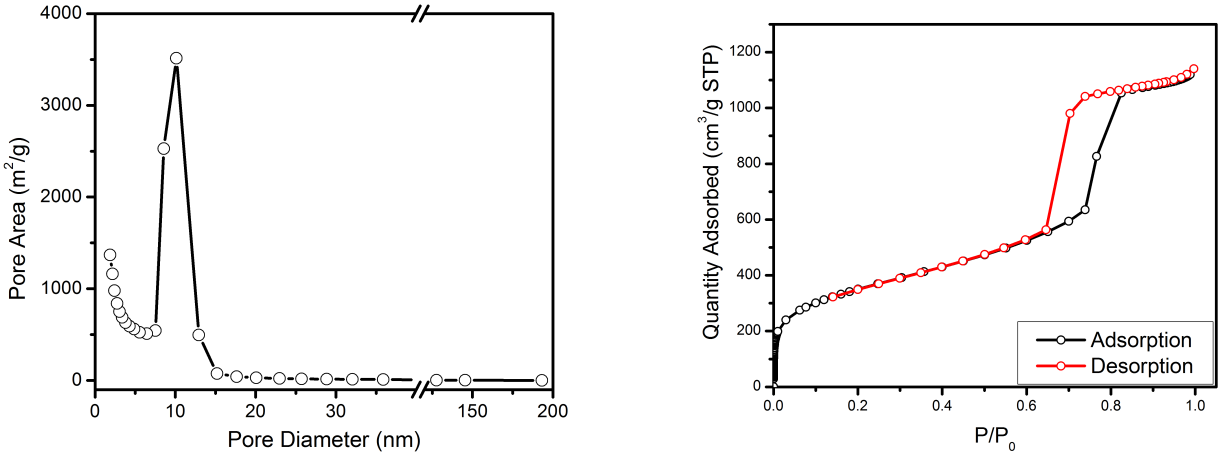

Figure 4.10: SBA-15 BET [Left] BJH determination of average pore sizes [Right] BET adsorption and desorption determination of surface area

Powder TGA was performed at a rate of 10^{o}C min^{-1}(Fig. 4.11). It should be noted that the silica sample (SA-SBA) showed extreme thermal stability as previously reported for cubic SBA-15.[117] Observation that the 50:50 wt% ratio of SA-(SBA-15:GO) decay values are exactly half-way between the TGA results obtained for pure SA-GO and pure SA-SBA provides another confirmation that the intended wt% ratio of nano-materials was maintained throughout the co-synthesis reaction. It is also seen that compared to GO, SA-GO boosts its high temperature weight by 5% indicating a high degree of functional species grafted on. With the aid of the polymer-templated silicon dioxide additive, a well dispersed nano-composite membrane will also be able to sustain higher temperature operation.[118,119]

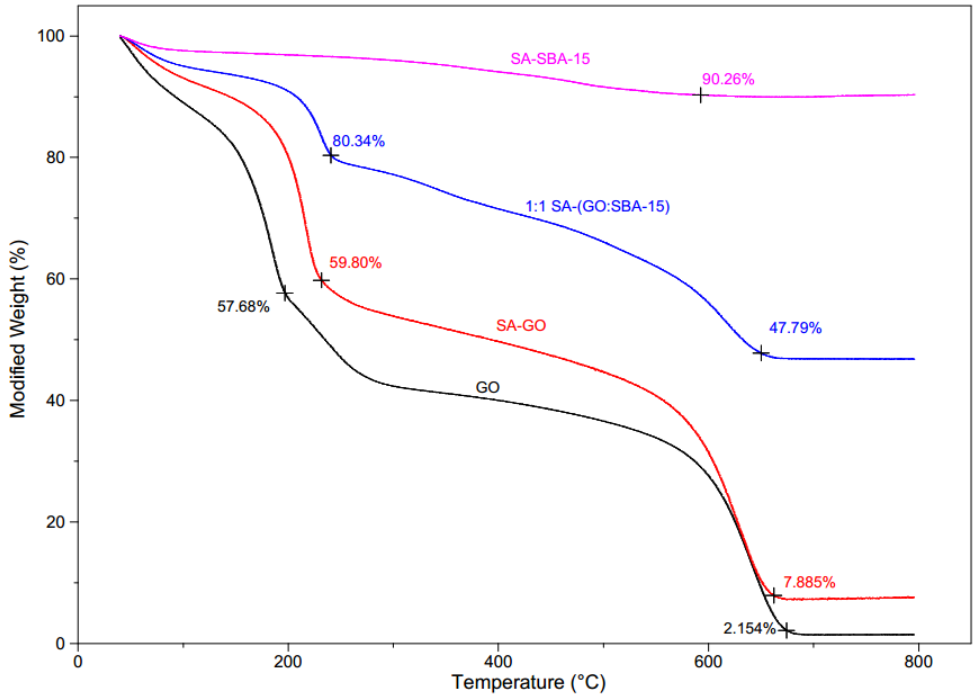

Figure 4.11: TGA of SA-GO and SA-SBA-15 powder ratios

4.3.2 Composite Membranes

For the purpose of investigating a novel humidity and temperature insensitive PEM, a variety of 5 wt% membranes were fabricated varying from 0 to 100 % in content ratios of co-functionalized GO and SBA-15 4.12. All membranes were cast in DMF and were homogenous and mechanically stable. One anomaly was the membrane cast with 5 wt% SA-SBA which would curl into a tube if not fully immersed in water. The initial hypothesis is that the porous structure is non-homogenous, possibly because of a higher concentration of dense particles near the bottom of the film compared to the upper surface. When removed from liquid, unequal water loss will contract the membrane along the less dense surface. The 33.3:66.7 wt% SA-(SBA:GO) membrane also showed some surface irregularity which was not present in other films or ratios.

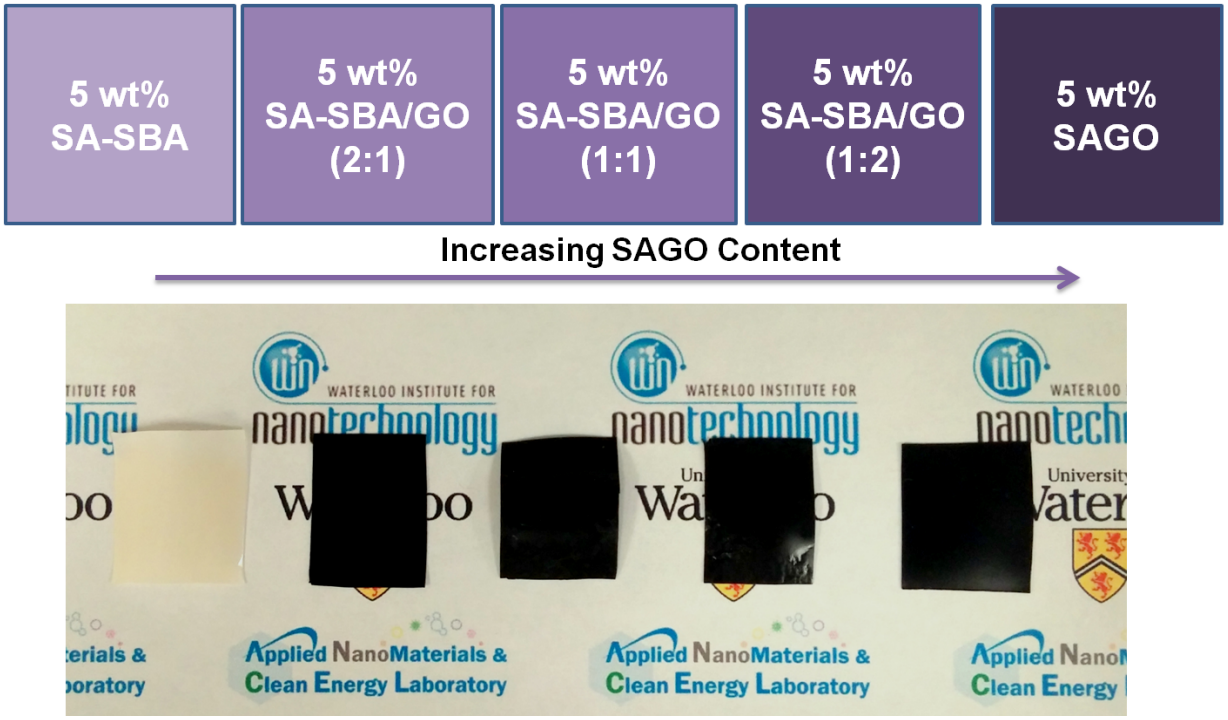

Figure 4.12: Physical membrane comparison with increasing SA-GO content versus SA-SBA

4.3.2.1 Morphology

SEM micrographs of the fabricated PFSA-nanomaterial membranes were collected by breaking membranes under liquid nitrogen and loading them vertically onto an SEM stage for cross-sectional analysis (Fig. 4.13 [Top]). All samples were gold sputtered with a 30 nm film prior to imaging. The PFSA-SA-SBA-15 membrane demonstrated two separate regimes, as shown in Figure 4.13 [Right] and confirmed by EDX mapping [Left]. Due to the relatively higher density of the mesoporous silica, it is possible that when forming into a membrane by solution casting these particles migrate to create a highly porous structure. The remaining membrane will resemble pure recast PFSA. The EDX image shows a highly dispersed distribution of fluorine (F) throughout the membrane, indicative of perfluorosulfonic content, while silicon (Si) is concentrated near the membrane base. This confirms the aforementioned theory whereby the upper and lower surface of the 5 wt% SA-SBA membrane would have different water loss and water uptake characteristics, causing it to bend once removed from a fully humidified environment. EDX mappings of other membranes containing both SA-GO and SA-SBA had homogeneous dispersion. There must exist an interaction between the mesoporous silica and graphene oxide nanoparticles for this change to occur.

A closer investigation into the 33:66 wt% (SBA-15:GO) membrane showed many 'wrapped-ball' structures present on the surface of the cross-sectional area. This is in high contrast to the rigid, sheet-like structure present in the SEM micrograph of PFSA-SA-GO. It is proposed that the cubic silica is wrapped by many exfoliated graphene oxide sheets while in solution. This larger structure is unable to migrate during membrane casting and is well dispersed into the membrane matrix. Further, the regularity of SA-GO is disrupted by the presence of SA-SBA which decreases the planar blocking of proton pathways and improves the network of hydrophilic domains within the bulk membrane.

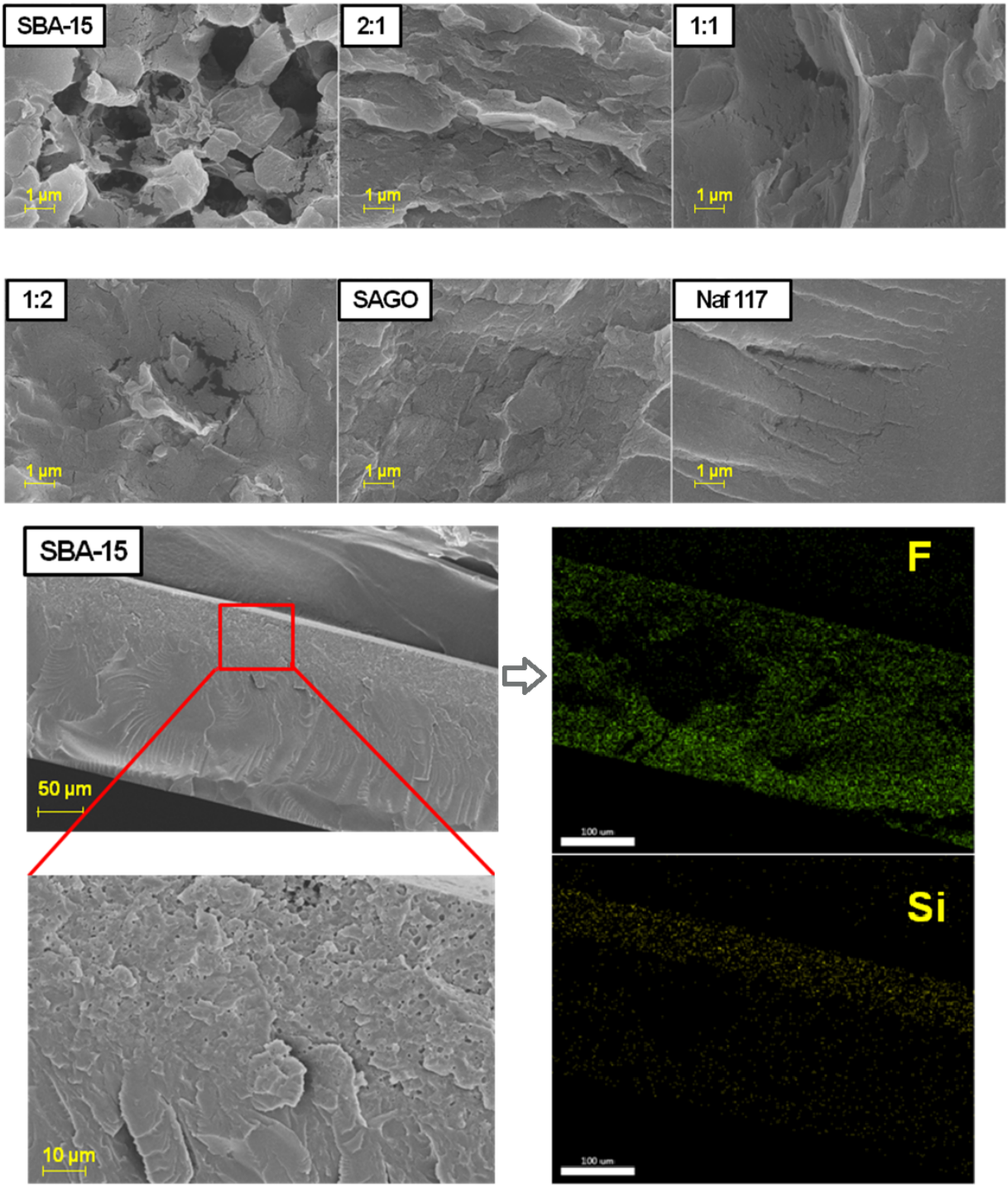

Figure 4.13: [Top] Comparison of cross-sectional SEM micrographs for varying ratios of SA-SBA and SA-GO in PFSA, also showing Nafion 117 ™[Left] Cross-sectional SEM micrographs of the 5 wt% SA-SBA membrane [Right] EDX Mapping of fluorine (F) and silicon (Si).

4.3.2.2 IEC, WU and Mobility

The water uptake and membrane swelling of all ratios of co-functionalized membrane outperformed either pure nanomaterial membrane (Fig. 4.14 [Left]). The ion exchange content was highest at a 33:66 wt% ratio of SA-(SBA-15:GO) and improved versus Nafion 117 ™(0.91 mmol g^{-1}).[77,120] The lower values with increasing SA-SBA is possibly due to the silica nanoparticle forming larger pore networks, resulting in a lower ion-exchange count per volume. The low IEC of PFSA-SA-GO is possibly influenced by its highly ordered structure, making ion exchange with Cl^- more difficult if graphene oxide films are closely stacked. Combining the through-plane conductivity measured at RT with the IEC and WU characterizations, the mobility of the membranes can be evaluated (Fig. 4.14 [Right]). This volcano peak demonstrates that the mixture of SA-SBA-15 and SA-GO is synergistic.

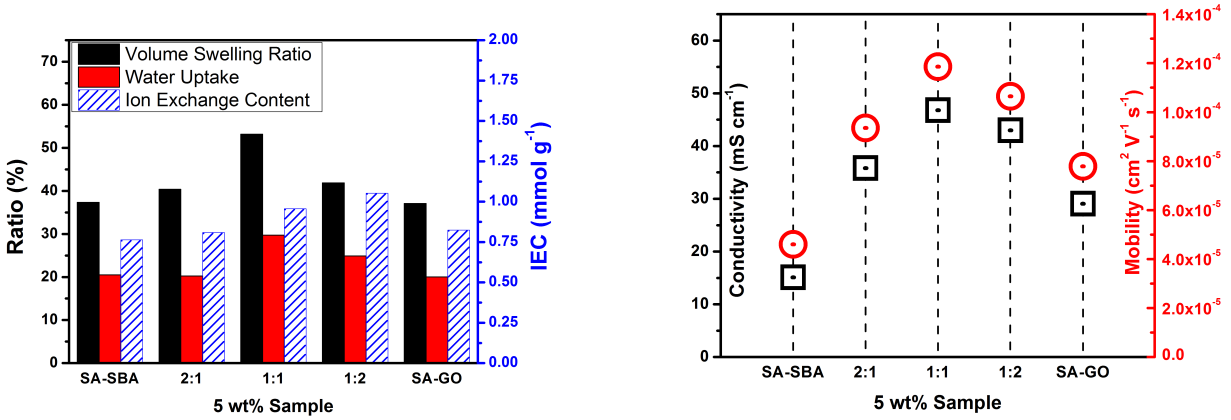

Figure 4.14: Membrane characteristics [Left] Swelling Ratio and Water Uptake of nanomaterial samples [Right] Through-plane ionic conductivity and mobility at 100 RH and 23^{o}C

4.3.2.3 Proton Conductivity

Membrane conductivity was determined by EIS measurements. Two methods were employed to evaluate the membranes across a range of humidities and temperatures. First,

at a fixed temperature (RT) the humidity was varied (Fig. 4.15). It is clear that the 33:66 wt% and 50:50 wt% membranes demonstrate improved conductivity across all humidity values, but are specifically improved at low humidity with a more than 5x improvement versus 5 wt% SA-GO. Second, measuring the conductivity at a fixed humidity and various temperatures to generate an Arrhenius plot (Fig. 4.15 [Right]), we are able to calculate the activation energy (G_{act}) as listed in Table 4.3. The activation energy indicates the energy barrier for proton migration based on the Grotthuss mechanism.[121,122] A good linear fit was present for the 1:1 ratio as well as for 5 wt% SA-GO. Focusing only on these two membranes, E_{act} appears to be inversely related to the hypothesis for enhanced mobility.

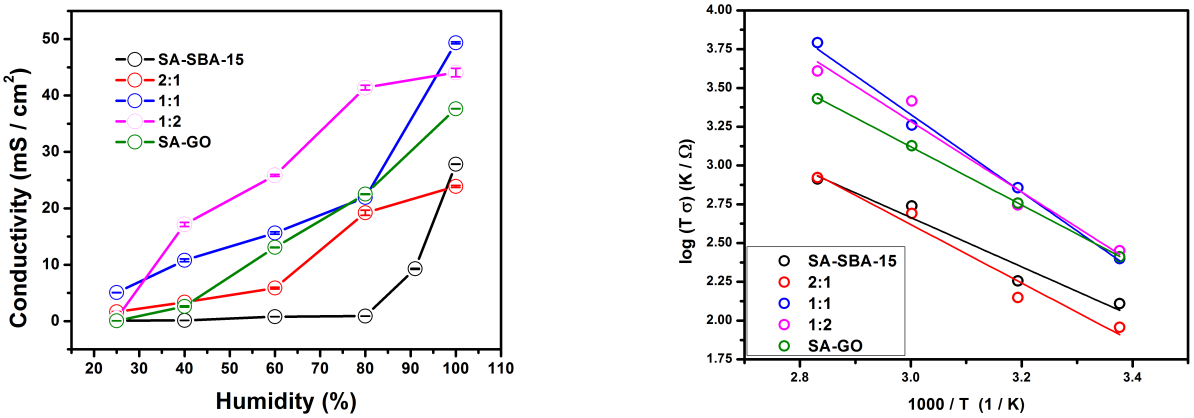

Figure 4.15: Membrane ionic conductivity [Left] Sample response versus RH [Right] Arrhenius plot of 100 RH conductivity from 20^{o}C to 80^{o}C with linear fit to determine activation energy.

Table 4.3: Arrhenius linear fit to determine activation energy

Sample Units	**Adj. R^2**	**E_{act}** kJ mol^{-}1	**E_{act}** eV
5 wt% SA-SBA-15	0.9367	13.206	0.137
2:1 SA-SBAGO	0.9534	15.677	0.162
1:1 SA-SBAGO	0.9912	20.817	0.216
1:2 SA-SBAGO	0.9467	18.926	0.196
5 wt% SA-GO	0.9996	15.595	0.162

Analysis of the presented data poses an interesting problem. How is it possible for ionic transport to require more energy, yet still demonstrate higher mobility? Both mobility and activation energy are a function of conductivity. Activation energy is related to the relative energy (in heat) which correlates to a change in the measured response. The ultimate goal is to provide a membrane with null change and sufficient conductivity across all temperatures. An Arrhenius plot of this theoretical membrane would have an infinitely large activation energy. Therefore, the increase in the activation energy is an indicator of a stable membrane response rather than proton immobility. The values reported above are also taken in wet (100 RH) conditions, much higher than would be present during typical operation. It is well known that with decreasing RH the activation energy will increase.[123] At activation energies between 0.5-0.9 eV, vehicle transport (H_3O^+) is the major mechanism.[124] Thus, the high mobility at low relative humidity indicates that significant vehicle transport is occurring, further that the addition of SA-SBAGO provides a significant source of this transport.

4.3.3 Full Cell Tests

Four days of accelerated degradation testing were performed on each of the nanocomposite membranes (Fig. 4.16).

To get a better understanding of the significance of these results, we can directly compare the recently created 5 wt% 50:50 SA-(SBA-15:GO) (1:1 SA-SBAGO for simplicity) membrane to the commercial Nafion 117 ™(Table 4.4). 1:1 SA-SBAGO sample demonstrates marginal ambient improvement in the relative decay rate, peak area and a slightly tailed response rate. However, immediately after exposure to the low humidity, harsh environment we see significant improvement in the response rate, stability of the peak area and peak height. These characteristics mark 1:1 SA-SBAGO as a candidate for long-term stability in normal conditions.

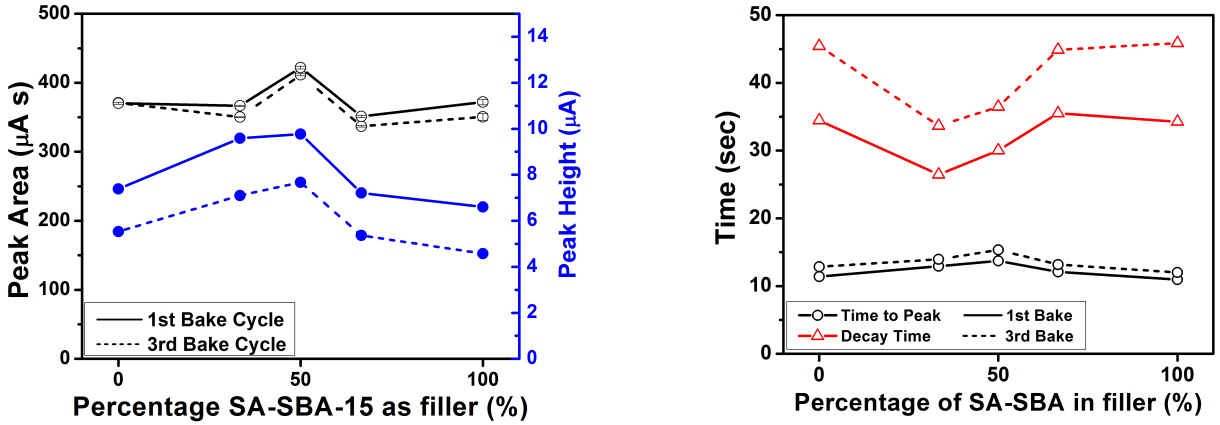

Figure 4.16: Membrane response characteristics for sulfonic acid functionalized SBA-15:GO ratios.

Table 4.4: Nafion 117 ™and 50:50 SA-(SBA-15:GO) response comparison humidified vs dehumidified

B1 - Bake Cycle 1	Humidified Overnight			After 2h 60°C		
B4 - Bake Cycle 4	Naf 117	SA-SBAGO	Dif [%]	Naf 117	SA-SBAGO	Dif [%]
Peak Height - B1	9.51	9.77	2.72	4.16	8.06	93.78
Peak Height - B4	6.56	7.39	12.75	2.87	6.17	114.93
Peak Area B1	378.01	422.05	11.65	424.17	431.19	1.66
Peak Area B4	359.71	414.84	15.32	409.31	425.94	4.06
Time to Peak B1	12.09	13.71	-13.40	32.29	16.75	48.13
Time to Peak B4	13.12	15.39	-17.30	42.54	19.27	54.71
Decay Time B1	26.96	30.02	-11.37	73.64	37.38	49.24
Decay Time B4	36.15	38.23	-5.76	103.72	47.94	53.78

4.3.3.1 Long Term Degradation

Long-term degradation was applied to selected samples using a commercial degradation method. The samples equilibrated overnight in a humidity chamber for the initial two weeks. They were tested every 3-4 days at 0.05 BAC using a commercial testing platform. It should be noted that the current area values here are not comparable to those performed on the home-built testing platform. The membranes were kept at ambient humidity excepting a test after 3 weeks where samples were left in the humidity chamber overnight, until 100 days had passed(Fig. 4.17). Although not as simple to discern in the raw data, applying a rough bezier spline to the data points a general trend for each sample can be observed. The fluctuating humidity conditions are measured in-lab before testing and vary due to weather and season. This mirrors the working conditions of FCS breathalyzers in the field where they are stored and periodically used to retrieve results. The 2:1 and 1:1 SA-SBAGO functionalized membranes demonstrated improved insensitivity to their environment. Over a period of 100 days, the 1:2 ratio maintained a valid response, followed by the 1:1 SA-SBAGO and then the 5 wt% SA-GO original.

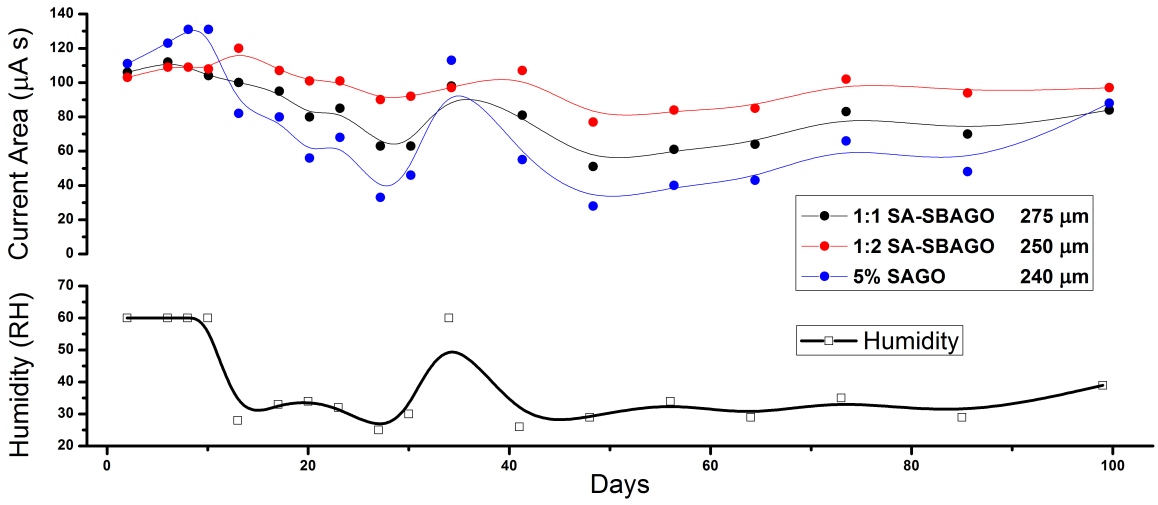

Figure 4.17: Membrane area change due to low-humidity environment. A Bezier spline applied to demonstrate general trend.

Chapter 5

Conclusions

5.1 Summary

There is a need for improved fuel cell sensors in the large and rapidly growing breathalyzer market.[25] Commercial units require frequent calibration due to water loss and the effect of the environment on a single sensor. The high cost of Nafion ™and its demonstrated conductivity change with water loss mandates investigation into alternative methods to enhance long-term durability of solid state fuel cell sensors. To date, very few publications have specifically focused on the challenges facing the fuel cell sensor industry with the majority of relevant research conducted into the hydrogen fuel cell with a focus on high power. Therefore, nanomaterial design and integration has a role in this small scale system where even slight improvement on the current commercial models is significant for judicial purposes.

To deal with the added issues of selectivity, sensitivity and membrane degradation a new testing platform was devised. Fuel cell sensors could be easily and repeatably tested on this platform, allowing for a more broad and complete investigation to occur. Sulfonated graphene oxide (SA-GO) was previously tested and demonstrated improved characteristics at low humidity conditions when integrated into a PFSA polymer.[26] However at high

weight percent integration in relatively thick membranes, a proton blocking effect was observed compared to pure PFSA. To recover the expected response profile as well as aid in the total charge transfer content, a mesoporous silica (SBA-15) was added as a spacer in the membranes. Graphene oxide sheets were observed to wrap around these particles, both aiding it the homogeneous dispersion as well as disrupting the layer-by-layer settling of pure exfoliated graphene oxide in solution. These two features resulted in a membrane response which is not only larger than Nafion 117 ™, but which demonstrates high response stability even in low-humidity conditions over the course of 100 days.

5.2 Future direction

In the original exploration, several weight percentages of nanomaterial content were explored. The choice of 5 wt% as a standard was due to the complexity in production as well as the observation that high nanomaterial contents of SA-GO alone in the solid state membrane would result in decreased performance or poor film formation. With the new results demonstrating stable films at 5 wt% and the "wrapping" synergy between SA-GO and SA-SBA-15, higher content can again be explored for higher water retention, ionic content and ultimately more reliable response performance.

Further, as 95% of the membrane film is still composed of the PFSA polymer, intrinsic water loss can be reduced by replacing or enveloping the polymeric ion conducting layer with low-loss polymer layers such as cellulose or polybenzimidazole. Finally, a thorough cost analysis of the nano-material synthesis procedure should be conducted before moving to any production stage. The cost of MPTMS, H_2O_2 and other materials mentioned in the synthesis procedure cannot be neglected.

References

[1] L. M. Haverhals. *Fuel Cells as Power Sources and Sensors*. PhD thesis, University of Iowa, 2008.

[2] Markets and Markets. Breath analyzers market - global industry analysis, size, share, growth, trends and forecast, 2013 - 2019, 2014. [Online; accessed 3-Nov-2015].

[3] Hadis Zarrin, Jing Fu, Gaopeng Jiang, Skylar Yoo, Jared Lenos, Michael Fowler, and Zhongwei Chen. Quaternized graphene oxide nanocomposites as fast hydroxide conductors. *ACS nano*, 9(2):2028–2037, 2015.

[4] Gaopeng Jiang, Maciej Goledzinowski, Felix JE Comeau, Hadis Zarrin, Gregory Lui, Jared Lenos, Alicia Veileux, Guihua Liu, Jing Zhang, Sahar Hemmati, et al. Free-standing functionalized graphene oxide solid electrolytes in electrochemical gas sensors. *Advanced Functional Materials*, 2016.

[5] R v. Singh. 2014 onca 293 (2016), 2016.

[6] Kurt M Dubowski. Alcohol determination in the clinical laboratory. *American Journal of Clinical Pathology*, 74(5):747–750, 1980.

[7] National Institute on Alcohol Abuse and Alcoholism. Alcohol overdose: The dangers of drinking too much, July 6, 2016 2015. [Online; accessed 6-July-2016].

[8] Kalen N Olson, Stephen W Smith, Julie S Kloss, Jeffrey D Ho, and Fred S Apple. Relationship between blood alcohol concentration and observable symptoms of intoxication in patients presenting to an emergency department. *Alcohol and alcoholism*, 48(4):386–389, 2013.

[9] AW Jones. Quantitative measurements of the alcohol concentration and the temperature of breath during a prolonged exhalation. *Acta Physiologica Scandinavica*, 114(3):407–412, 1982.

[10] Jrn Ueberfeld, Hugo Zbinden, Nicolas Gisin, and Jean-Paul Pellaux. Determination of henrys constant using a photoacoustic sensor. *The Journal of Chemical Thermodynamics*, 33(7):755–764, 2001.

[11] AW Jones. Determination of liquid/air partition coefficients for dilute solutions of ethanol in water, whole blood, and plasma. *Journal of analytical toxicology*, 7(4):193–197, 1983.

[12] EN Harger, Robert B Forney, and Helen B Barnes. Estimation of the level of blood alcohol from analysis of breath. *Translational Research*, 36(2):306–318, 1950.

[13] TA Alobaidi, DW Hill, and JP Payne. Significance of variations in blood: breath partition coefficient of alcohol. *Br Med J*, 2(6050):1479–1481, 1976.

[14] Hernan F Gomez, Laura Moore, Patrick McKinney, Scott Phillips, Hulya Guven, and Jeffrey Brent. Elevation of breath ethanol measurements by metered-dose inhalers. *Annals of emergency medicine*, 25(5):608–611, 1995.

[15] Alan Wayne Jones and Lars Andersson. Variability of the blood/breath alcohol ratio in drinking drivers. *Journal of Forensic Science*, 41(6):916–921, 1996.

[16] Recommended standards and procedures of the canadian society of forensic science alcohol test committee. *Canadian Society of Forensic Science Journal*, 36(3):101–127, 2003.

[17] Robert F Borkenstein and HW Smith. The breathalyzer and its applications. *Medicine, Science and the Law*, 2(1):13–22, 1961.

[18] R.N. Harger. Apparatus for measuring alcohol content of gases, 1959.

[19] MF Mason and Kurt M Dubowski. Breath-alcohol analysis: uses, methods, and some forensic problemsreview and opinion. *Journal of Forensic Science*, 21(1):9–41, 1976.

[20] Werner K Adrian and Robert F Borkenstein. Determination of the alcohol content of blood, 1983.

[21] TA Alobaidi, DW Hill, and JP Payne. Significance of variations in blood: breath partition coefficient of alcohol. *Br Med J*, 2(6050):1479–1481, 1976.

[22] T. Naoyoshi. Gas-detecting device, 1971.

[23] C. Lamy, A. Lima, V. LeRhun, F. Delime, C. Coutanceau, and J. M. Leger. Recent advances in the development of direct alcohol fuel cells (dafc). *Journal of Power Sources*, 105(2):283–296, 2002. 538GA Times Cited:580 Cited References Count:53.

[24] Shuqin Song and Panagiotis Tsiakaras. Recent progress in direct ethanol proton exchange membrane fuel cells (de-pemfcs). *Applied Catalysis B: Environmental*, 63(3-4):187–193, 2006.

[25] Markets and Markets. Breath analyzers market by technology, by application, by end user - analysis & global forecast to 2019, 2014. [Online; accessed 3-Nov-2015].

[26] TechNavio. Global alcohol detection breath analyzers market 2014-2018, 2014. [Online; accessed 3-Nov-2015].

[27] TechNavio. Global breath analyzers market 2014-2018, 2014. [Online; accessed 3-Nov-2015].

[28] Hadis Zarrin, Drew Higgins, Yu Jun, Zhongwei Chen, and Michael Fowler. Functionalized graphene oxide nanocomposite membrane for low humidity and high temperature proton exchange membrane fuel cells. *The Journal of Physical Chemistry C*, 115(42):20774–20781, 2011.

[29] DC Lee, HN Yang, SH Park, and WJ Kim. Nafion/graphene oxide composite membranes for low humidifying polymer electrolyte membrane fuel cell. *Journal of Membrane Science*, 452:20–28, 2014.

[30] Hung-Chung Chien, Li-Duan Tsai, Chiu-Ping Huang, Chi-yun Kang, Jiunn-Nan Lin, and Feng-Chih Chang. Sulfonated graphene oxide/nafion composite membranes for high-performance direct methanol fuel cells. *international journal of hydrogen energy*, 38(31):13792–13801, 2013.

[31] Bong Gill Choi, Yun Suk Huh, Young Chul Park, Doo Hwan Jung, Won Hi Hong, and HoSeok Park. Enhanced transport properties in polymer electrolyte composite membranes with graphene oxide sheets. *Carbon*, 50(15):5395–5402, 2012.

[32] KT Adjemian, SJ Lee, S Srinivasan, J Benziger, and AB Bocarsly. Silicon oxide nafion composite membranes for proton-exchange membrane fuel cell operation at 80-140 c. *Journal of the Electrochemical Society*, 149(3):A256–A261, 2002.

[33] DH Jung, SY Cho, DH Peck, DR Shin, and JS Kim. Performance evaluation of a nafion/silicon oxide hybrid membrane for direct methanol fuel cell. *Journal of power sources*, 106(1):173–177, 2002.

[34] Zhi-Gang Shao, Prabhuram Joghee, and I-Ming Hsing. Preparation and characterization of hybrid nafion–silica membrane doped with phosphotungstic acid for high temperature operation of proton exchange membrane fuel cells. *Journal of Membrane Science*, 229(1):43–51, 2004.

[35] Zhi-Gang Shao, Hongfeng Xu, Mingqiang Li, and I-Ming Hsing. Hybrid nafion–inorganic oxides membrane doped with heteropolyacids for high temperature operation of proton exchange membrane fuel cell. *Solid State Ionics*, 177(7):779–785, 2006.

[36] A Sacca, A Carbone, E Passalacqua, A Depifanio, S Licoccia, E Traversa, E Sala, F Traini, and R Ornelas. Nafion–tio 2 hybrid membranes for medium temperature polymer electrolyte fuel cells (pefcs). *Journal of power sources*, 152:16–21, 2005.

[37] May Barclay Satterfield. *Mechanical and water sorption properties of Nafion and composite Nafion/titanium dioxide membranes for polymer electrolyte membrane fuel cells*. PhD thesis, Citeseer, 2007.

[38] Zhongwei Chen, Brett Holmberg, Wenzhen Li, Xin Wang, Weiqiao Deng, Ronnie Munoz, and Yushan Yan. Nafion/zeolite nanocomposite membrane by in situ crystallization for a direct methanol fuel cell. *Chemistry of Materials*, 18(24):5669–5675, 2006.

[39] Dong-Hoon Son, Raj Kishore Sharma, Yong-Gun Shul, and Hansung Kim. Preparation of pt/zeolite–nafion composite membranes for self-humidifying polymer electrolyte fuel cells. *Journal of power sources*, 165(2):733–738, 2007.

[40] Brett A Holmberg, Xin Wang, and Yushan Yan. Nanocomposite fuel cell membranes based on nafion and acid functionalized zeolite beta nanocrystals. *Journal of membrane science*, 320(1):86–92, 2008.

[41] H Chang, JR Kim, JH Cho, HK Kim, and KH Choi. Materials and processes for small fuel cells. *Solid State Ionics*, 148(3):601–606, 2002.

[42] S Sasikala, S Vinod Selvaganesh, AK Sahu, A Carbone, and E Passalacqua. Block co-polymer templated mesoporous carbon–nafion hybrid membranes for polymer electrolyte fuel cells under reduced relative humidity. *Journal of Membrane Science*, 499:503–514, 2016.

[43] JS Wainright, J-T Wang, D Weng, RF Savinell, and M Litt. Acid-doped polybenzimidazoles: a new polymer electrolyte. *Journal of the Electrochemical Society*, 142(7):L121–L123, 1995.

[44] David Mecerreyes, Hans Grande, Oscar Miguel, Estibalitz Ochoteco, Rebeca Marcilla, and Igor Cantero. Porous polybenzimidazole membranes doped with phosphoric acid: highly proton-conducting solid electrolytes. *Chemistry of materials*, 16(4):604–607, 2004.

[45] Hadis Zarrin, Michael Fowler, and Zhongwei Chen. Highly anion-conducting porous polymer electrolyte membrane for alkaline fuel cells. *ECS Transactions*, 50(2):2083–2089, 2012.

[46] S. C. Kumbharkar, Md Nazrul Islam, R. A. Potrekar, and U. K. Kharul. Variation in acid moiety of polybenzimidazoles: Investigation of physico-chemical properties towards their applicability as proton exchange and gas separation membrane materials. *Polymer*, 50(6):1403–1413, 2009.

[47] Hiroshi Akita, Masao Ichikawa, Masaru Iguchi, and Hiroyuki Oyanagi. Sulfonic acid group-containing polyvinyl alcohol, solid polymer electrolyte, composite polymer membrane, method for producing the same and electrode, February 25 2003. US Patent 6,523,699.

[48] Dae Sik Kim, Ho Bum Park, Ji Won Rhim, and Young Moo Lee. Preparation and characterization of crosslinked pva/sio 2 hybrid membranes containing sulfonic acid groups for direct methanol fuel cell applications. *Journal of Membrane Science*, 240(1):37–48, 2004.

[49] P. Millet, A. Michas, and R. Durand. A solid polymer electrolyte-based ethanol gas sensor. *Journal of Applied Electrochemistry*, 26(9):933–937, 1996. Vh213 Times Cited:22 Cited References Count:23.

[50] Flavio Colmati, Ermete Antolini, and Ernesto R. Gonzalez. Effect of temperature on the mechanism of ethanol oxidation on carbon supported pt, ptru and pt3sn electrocatalysts. *Journal of Power Sources*, 157(1):98–103, 2006.

[51] K. C. Kim, S. M. Cho, and H. G. Choi. Detection of ethanol gas concentration by fuel cell sensors fabricated using a solid polymer electrolyte. *Sensors and Actuators B-Chemical*, 67(1-2):194–198, 2000. 340UH Times Cited:9 Cited References Count:7.

[52] Weijiang Zhou, Zhenhua Zhou, Shuqin Song, Wenzhen Li, Gongquan Sun, Panagiotis Tsiakaras, and Qin Xin. Pt based anode catalysts for direct ethanol fuel cells. *Applied Catalysis B: Environmental*, 46(2):273–285, 2003.

[53] WJ Zhou, Sh Q Song, W Zh Li, Zh H Zhou, GQ Sun, Q Xin, S Douvartzides, and P Tsiakaras. Direct ethanol fuel cells based on ptsn anodes: the effect of sn content on the fuel cell performance. *Journal of Power Sources*, 140(1):50–58, 2005.

[54] SQ Song, WJ Zhou, ZH Zhou, LH Jiang, GQ Sun, Q Xin, V Leontidis, S Kontou, and P Tsiakaras. Direct ethanol pem fuel cells: the case of platinum based anodes. *International Journal of Hydrogen Energy*, 30(9):995–1001, 2005.

[55] RA Rightmire, RL Rowland, DL Boos, and DL Beals. Ethyl alcohol oxidation at platinum electrodes. *Journal of The Electrochemical Society*, 111(2):242–247, 1964.

[56] AR Blake, AT Kuhn, and JG Sunderland. The low potential oxidation of ethanol on bright platinum. *Journal of The Electrochemical Society*, 120(4):492–497, 1973.

[57] Klaus-Dieter Kreuer, Thomas Dippel, Wolfgang Meyer, and Joachim Maier. Nafion® membranes: Molecular diffusion, proton conductivity and proton conduction mechanism. In *MRS Proceedings*, volume 293, page 273. Cambridge Univ Press, 1992.

[58] BD Cahan and JS Wainright. Ac impedance investigations of proton conduction in nafion. *Journal of the Electrochemical Society*, 140(12):L185–L186, 1993.

[59] Felix N. Buchi and Gunther G. Scherer. Investigation of the transversal water profile in nafion membranes in polymer electrolyte fuel cells. *Journal of The Electrochemical Society*, 148(3):A183, 2001.

[60] Peter C Rieke and Nicholas E Vanderborgh. Temperature dependence of water content and proton conductivity in polyperfluorosulfonic acid membranes. *Journal of membrane Science*, 32(2-3):313–328, 1987.

[61] A Sungpet. Reduction of alcohol permeation through nafion® by polypyrrole. *Journal of membrane science*, 226(1):131–134, 2003.

[62] Chieh-Hao Wan and Chin-Lou Chen. Mitigating ethanol crossover in defc: a composite anode with a thin layer of pt 50–sn 50 nanoparticles directly deposited into nafion® membrane surface. *international journal of hydrogen energy*, 34(23):9515–9522, 2009.

[63] Shuqin Song, Guoxiong Wang, Weijiang Zhou, Xinsheng Zhao, Gongquan Sun, Qin Xin, S Kontou, and P Tsiakaras. The effect of the mea preparation procedure on both ethanol crossover and defc performance. *Journal of power sources*, 140(1):103–110, 2005.

[64] S Murthy Tadavarthy, JAMES H MOLLER, and KURT AMPLATZ. Polyvinyl alcohol (ivalon)a new embolic material. *American Journal of Roentgenology*, 125(3):609–616, 1975.

[65] J.W.T. Grubb. Fuel cell, November 17 1959. US Patent 2,913,511.

[66] Mu-Rong Yang and Ko-Shao Chen. Humidity sensors using polyvinyl alcohol mixed with electrolytes. *Sensors and Actuators B: Chemical*, 49(3):240–247, 1998.

[67] Ainhoa Gastón, Fátima Pérez, and Joaquín Sevilla. Optical fiber relative-humidity sensor with polyvinyl alcohol film. *Applied optics*, 43(21):4127–4132, 2004.

[68] K. T. Adjemian, R. Dominey, L. Krishnan, H. Ota, P. Majsztrik, T. Zhang, B. Kirby, L. Gatto, M. Velo-Simpson, J. Leahy, S. Srinivasan, J. B. Benziger, and A. B. Bocarsly.

Function and characterization of metal oxide-nafion composite membranes for elevated-temperature h2/o2 pem fuel cells. *Chemical Materials*, 18:11, 2006.

[69] M. Amjadi, S. Rowshanzamir, S. J. Peighambardoust, M. G. Hosseini, and M. H. Eikani. Investigation of physical properties and cell performance of nafion/tio2 nanocomposite membranes for high temperature pem fuel cells. *International Journal of Hydrogen Energy*, 35(17):9252–9260, 2010.

[70] Chennan Li, Gongquan Sun, Suzhen Ren, Jin Liu, Qi Wang, Zhimou Wu, Hai Sun, and Wei Jin. Casting nafionsulfonated organosilica nano-composite membranes used in direct methanol fuel cells. *Journal of Membrane Science*, 272(1-2):50–57, 2006.

[71] Yu Jun, Hadis Zarrin, Michael Fowler, and Zhongwei Chen. Functionalized titania nanotube composite membranes for high temperature proton exchange membrane fuel cells. *International Journal of Hydrogen Energy*, 36(10):6073–6081, 2011.

[72] Ruichun Jiang, H Russell Kunz, and James M Fenton. Composite silica/nafion® membranes prepared by tetraethylorthosilicate sol–gel reaction and solution casting for direct methanol fuel cells. *Journal of Membrane Science*, 272(1):116–124, 2006.

[73] Bruno R Matos, Roberta A Isidoro, Elisabete I Santiago, Marcelo Linardi, Andre S Ferlauto, Ana C Tavares, and Fabio C Fonseca. In situ fabrication of nafion–titanate hybrid electrolytes for high-temperature direct ethanol fuel cell. *The Journal of Physical Chemistry C*, 117(33):16863–16870, 2013.

[74] Michael A Hickner, Hossein Ghassemi, Yu Seung Kim, Brian R Einsla, and James E McGrath. Alternative polymer systems for proton exchange membranes (pems). *Chemical reviews*, 104(10):4587–4612, 2004.

[75] Dong Won Shin, Na Rae Kang, Kang Hyuck Lee, Doo Hee Cho, Ji Hoon Kim, Won Hyo Lee, and Young Moo Lee. Proton conducting, composite sulfonated polymer membrane for medium temperature and low relative humidity fuel cells. *Journal of Power Sources*, 262:162–168, 2014.

[76] Yao He, Cuiyan Tong, Lei Geng, Lingdi Liu, and Changli L. Enhanced performance of the sulfonated polyimide proton exchange membranes by graphene oxide: Size effect of graphene oxide. *Journal of Membrane Science*, 458:36–46, 2014.

[77] R. S. Bhavsar, S. B. Nahire, M. S. Kale, S. G. Patil, P. P. Aher, R. A. Bhavsar, and U. K. Kharul. Polybenzimidazoles based on 3,3-diaminobenzidine and aliphatic dicarboxylic acids: Synthesis and evaluation of physico-chemical properties towards their applicability as proton exchange and gas separation membrane material. 2010.

[78] Feng Wang, Michael Hickner, Yu Seung Kim, Thomas A Zawodzinski, and James E McGrath. Direct polymerization of sulfonated poly (arylene ether sulfone) random (statistical) copolymers: candidates for new proton exchange membranes. *Journal of Membrane Science*, 197(1):231–242, 2002.

[79] Qunhui Guo, Peter N Pintauro, Hao Tang, and Sally O'Connor. Sulfonated and crosslinked polyphosphazene-based proton-exchange membranes. *Journal of Membrane Science*, 154(2):175–181, 1999.

[80] Huixiong Xie, Dan Tao, Xiongzhi Xiang, Yangxing Ou, Xiaojun Bai, and Lei Wang. Synthesis and properties of highly branched star-shaped sulfonated block poly (arylene ether) s as proton exchange membranes. *Journal of Membrane Science*, 473:226–236, 2015.

[81] Prabhakar Singh and Nguyen Q Minh. Solid oxide fuel cells: technology status. *International Journal of Applied Ceramic Technology*, 1(1):5–15, 2004.

[82] Jianbing Huang, Fucheng Xie, Cheng Wang, and Zongqiang Mao. Development of solid oxide fuel cell materials for intermediate-to-low temperature operation. *international journal of hydrogen energy*, 37(1):877–883, 2012.

[83] Bruno L Augusto, Fábio B Noronha, Fabio C Fonseca, Francisco N Tabuti, Rita C Colman, and Lisiane V Mattos. Nickel/gadolinium-doped ceria anode for direct ethanol

solid oxide fuel cell. *International Journal of Hydrogen Energy*, 39(21):11196–11209, 2014.

[84] G. Korotcenkov. Chemical sensors comprehensive sensor technologies - volume 5: Electrochemical and optical sensors, 2011.

[85] HL Yeager and A Steck. Cation and water diffusion in nafion ion exchange membranes: influence of polymer structure. *Journal of the Electrochemical Society*, 128(9):1880–1884, 1981.

[86] Anne-Laure Rollet, Olivier Diat, and Gérard Gebel. A new insight into nafion structure. *The Journal of Physical Chemistry B*, 106(12):3033–3036, 2002.

[87] Thomas A Zawodzinski, Charles Derouin, Susan Radzinski, Ruth J Sherman, Van T Smith, Thomas E Springer, and Shimshon Gottesfeld. Water uptake by and transport through nafion® 117 membranes. *Journal of the electrochemical society*, 140(4):1041–1047, 1993.

[88] František Opekar. An amperometric solid-state sensor for nitrogen dioxide based on a solid polymer electrolyte. *Electroanalysis*, 4(2):133–138, 1992.

[89] M Casciola, G Alberti, M Sganappa, and R Narducci. On the decay of nafion proton conductivity at high temperature and relative humidity. *Journal of Power Sources*, 162(1):141–145, 2006.

[90] Richard S Yeo. Ion clustering and proton transport in nafion membranes and its applications as solid polymer electrolyte. *Journal of the Electrochemical Society*, 130(3):533–538, 1983.

[91] Tatsuhiro Okada, Steffen Møller-Holst, Oddvar Gorseth, and Signe Kjelstrup. Transport and equilibrium properties of nafion® membranes with h+ and na+ ions. *Journal of Electroanalytical Chemistry*, 442(1):137–145, 1998.

[92] Marcella Cappadonia, J Wilhelm Erning, Seyedeh M Saberi Niaki, and Ulrich Stimming. Conductance of nafion 117 membranes as a function of temperature and water content. *Solid State Ionics*, 77:65–69, 1995.

[93] Zijie Lu, Georgios Polizos, Digby D Macdonald, and E Manias. State of water in perfluorosulfonic ionomer (nafion 117) proton exchange membranes. *Journal of The Electrochemical Society*, 155(2):B163–B171, 2008.

[94] M. A. Anghel. Quality assurance in breath-alcohol analysis. *U.P.B Science Bulletin, Series A.*, 68(2):61–71, 2006.

[95] SC Chang, JR Stetter, and CS Cha. Amperometric gas sensors. *Talanta*, 40(4):461–477, 1993.

[96] Antony Manolis. The diagnostic potential of breath analysis. *Clinical chemistry*, 29(1):5–15, 1983.

[97] John M Sedlak and Keith F Blurton. Electrochemical determination of hydrogen sulphide in air. *Talanta*, 23(6):445–448, 1976.

[98] Y. Zhu, S. Murali, W. Cai, X. Li, J. W. Suk, J. R. Potts, and R. S. Ruoff. Graphene and graphene oxide: synthesis, properties, and applications. *Adv Mater*, 22(35):3906–24, 2010. Zhu, Yanwu Murali, Shanthi Cai, Weiwei Li, Xuesong Suk, Ji Won Potts, Jeffrey R Ruoff, Rodney S Germany Deerfield Beach, Fla. Adv Mater. 2010 Sep 15;22(35):3906-24. doi: 10.1002/adma.201001068.

[99] Aiping Yu, Isaac Roes, Aaron Davies, and Zhongwei Chen. Ultrathin, transparent, and flexible graphene films for supercapacitor application. *Applied physics letters*, 96(25):253105, 2010.

[100] William S Hummers Jr and Richard E Offeman. Preparation of graphitic oxide. *Journal of the American Chemical Society*, 80(6):1339–1339, 1958.

[101] L. M. Yang, Y. J. Wang, G. S. Luo, and Y. Y. Dai. Functionalization of sba-15 mesoporous silica with thiol or sulfonic acid groups under the crystallization conditions. *Microporous and Mesoporous Materials*, 84(1-3):275–282, 2005.

[102] Lakshi Saikia, Darbha Srinivas, and Paul Ratnasamy. Comparative catalytic activity of mn(salen) complexes grafted on sba-15 functionalized with amine, thiol and sulfonic acid groups for selective aerial oxidation of limonene. *Microporous and Mesoporous Materials*, 104(1-3):225–235, 2007.

[103] Vellaichamy Ganesan and Alain Walcarius. Surfactant templated sulfonic acid functionalized silica microspheres as new efficient ion exchangers and electrode modifiers. *Langmuir*, 20(9):3632–3640, 2004.

[104] Karthikeyan Krishnamoorthy, Murugan Veerapandian, Kyusik Yun, and S-J Kim. The chemical and structural analysis of graphene oxide with different degrees of oxidation. *Carbon*, 53:38–49, 2013.

[105] Dongyuan Zhao, Jinyu Sun, Quanzhi Li, and Galen D Stucky. Morphological control of highly ordered mesoporous silica sba-15. *Chemistry of Materials*, 12(2):275–279, 2000.

[106] Anne Galarneau, Hélène Cambon, Francesco Di Renzo, and François Fajula. True microporosity and surface area of mesoporous sba-15 silicas as a function of synthesis temperature. *Langmuir*, 17(26):8328–8335, 2001.

[107] P. Knauth, L. Pasquini, B. Maranesi, K. Pelzer, R. Polini, and M. L. Di Vona. Proton mobility in sulfonated polyetheretherketone (speek): Influence of thermal crosslinking and annealing. *Fuel Cells*, 13(1):79–85, 2013.

[108] T. Workman. The science behind breath testing. *UMass Law Review*, 7(110):143–180, 2012.

[109] RN Harger, BB Raney, EG Bridwell, and Mary F Kitchel. The partition ratio of alcohol between air and water, urine and blood; estimation and identification of alcohol in these

liquids from analysis of air equilibrated with them. *Journal of biological chemistry*, 183(1):197–213, 1950.

[110] Kurt M Dubowski. Breath analysis as a technique in clinical chemistry. *Clinical chemistry*, 20(8):966–972, 1974.

[111] F t Franks and DJG Ives. The structural properties of alcohol–water mixtures. *Quarterly Reviews, Chemical Society*, 20(1):1–44, 1966.

[112] Kurt M Dubowski. Breath-alcohol simulators: scientific basis and actual performance. *Journal of Analytical Toxicology*, 3(5):177–182, 1979.

[113] I Nicotera, C Simari, L Coppola, P Zygouri, D Gournis, S Brutti, F Demetrio Minuto, AS Aricò, D Sebastian, and V Baglio. Sulfonated graphene oxide platelets in nafion nanocomposite membrane: advantages for application in direct methanol fuel cells. *The Journal of Physical Chemistry C*, 118(42):24357–24368, 2014.

[114] Kai Feng, Beibei Tang, and Peiyi Wu. Sulfonated graphene oxide–silica for highly selective nafion-based proton exchange membranes. *Journal of Materials Chemistry A*, 2(38):16083–16092, 2014.

[115] D. C. Marcano, D. V. Kosynkin, J. M. Berlin, A. Sinitskii, Z. Sun, A. Slesarev, L. B. Alemany, W. Lu, and J. M. Tour. Improved synthesis of graphene oxide. *ACS Nano*, 4(8):4806–14, 2010. Marcano, Daniela C Kosynkin, Dmitry V Berlin, Jacob M Sinitskii, Alexander Sun, Zhengzong Slesarev, Alexander Alemany, Lawrence B Lu, Wei Tour, James M ACS Nano. 2010 Aug 24;4(8):4806-14. doi: 10.1021/nn1006368.

[116] A. M. Dimiev and J. M. Tour. Mechanism of graphene oxide formation. *ACS Nano*, 8(3):3060–8, 2014. Dimiev, Ayrat M Tour, James M ACS Nano. 2014 Mar 25;8(3):3060-8. doi: 10.1021/nn500606a. Epub 2014 Mar 6.

[117] Michal Kruk, Mietek Jaroniec, Chang Hyun Ko, and Ryong Ryoo. Characterization of the porous structure of sba-15. *Chemistry of materials*, 12(7):1961–1968, 2000.

[118] Haolin Tang, Zhaohui Wan, Mu Pan, and San Ping Jiang. Self-assembled nafion–silica nanoparticles for elevated-high temperature polymer electrolyte membrane fuel cells. *Electrochemistry Communications*, 9(8):2003–2008, 2007.

[119] Yoichi Tominaga, In-Chul Hong, Shigeo Asai, and Masao Sumita. Proton conduction in nafion composite membranes filled with mesoporous silica. *Journal of power sources*, 171(2):530–534, 2007.

[120] Qingtao Luo, Huaming Zhang, Jian Chen, Peng Qian, and Yunfeng Zhai. Modification of nafion membrane using interfacial polymerization for vanadium redox flow battery applications. *Journal of Membrane Science*, 311(1):98–103, 2008.

[121] Stephen J Paddison and Reginald Paul. The nature of proton transport in fully hydrated nafion®. *Physical Chemistry Chemical Physics*, 4(7):1158–1163, 2002.

[122] Pyoungho Choi, Nikhil H Jalani, and Ravindra Datta. Thermodynamics and proton transport in nafion ii. proton diffusion mechanisms and conductivity. *Journal of the electrochemical society*, 152(3):E123–E130, 2005.

[123] F Damay and LC Klein. Transport properties of nafion composite membranes for proton-exchange membranes fuel cells. *Solid State Ionics*, 162:261–267, 2003.

[124] Xiaoqiang Liang, Feng Zhang, Wei Feng, Xiaoqin Zou, Chengji Zhao, Hui Na, Cong Liu, Fuxing Sun, and Guangshan Zhu. From metal–organic framework (mof) to mof–polymer composite membrane: enhancement of low-humidity proton conductivity. *Chemical Science*, 4(3):983–992, 2013.

[125] Anthony F Sammells, Ronald L Cook, James H White, Jeremy J Osborne, and Robert C MacDuff. Rational selection of advanced solid electrolytes for intermediate temperature fuel cells. *Solid State Ionics*, 52(1-3):111–123, 1992.

APPENDICES

Appendix A

Drawings, Designs and Schematics for Fuel Cell Sensor Test Components

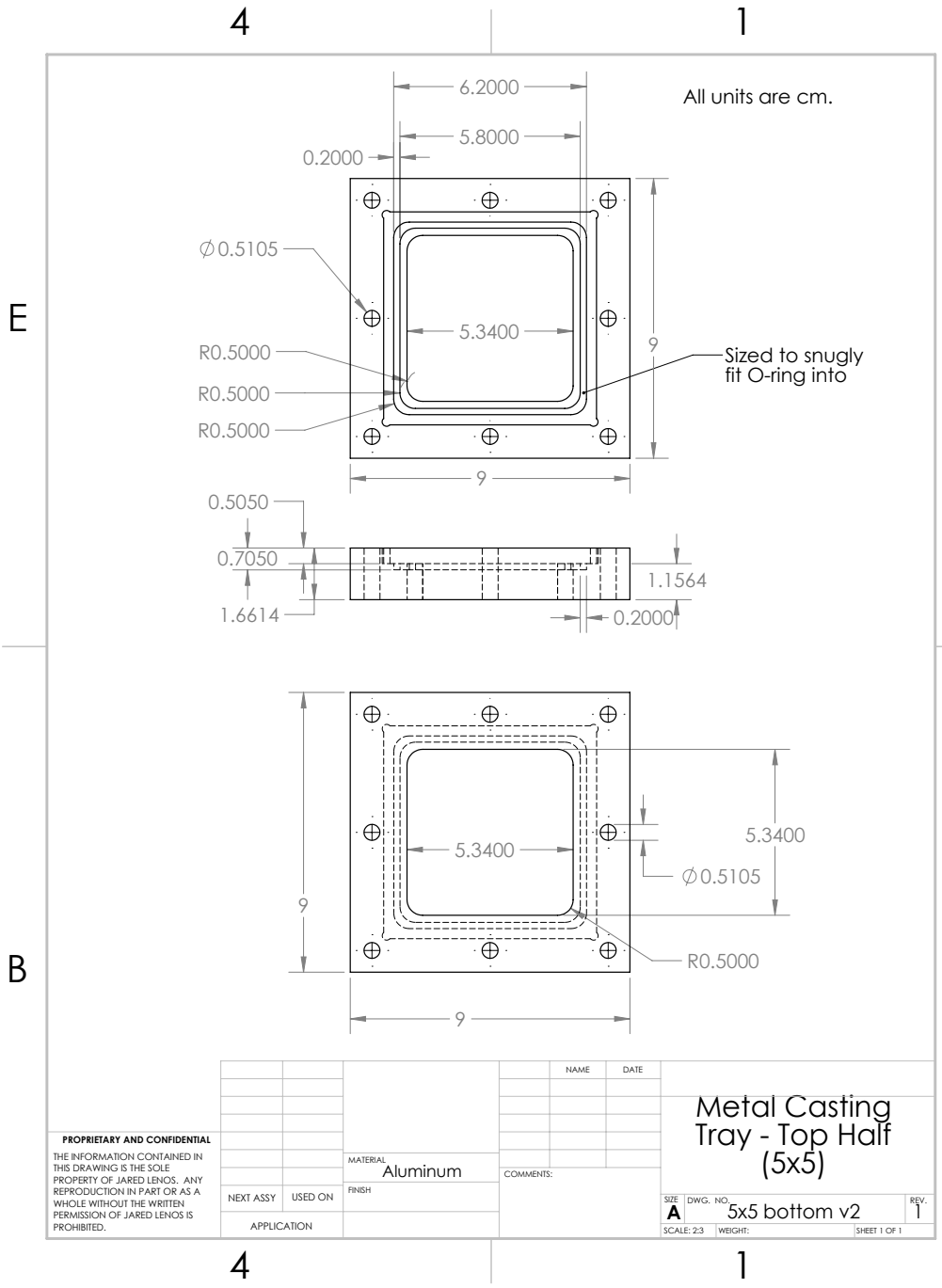

Figure A.1: Solidworks design of the 28.5 cm^2 casting tray upper layer

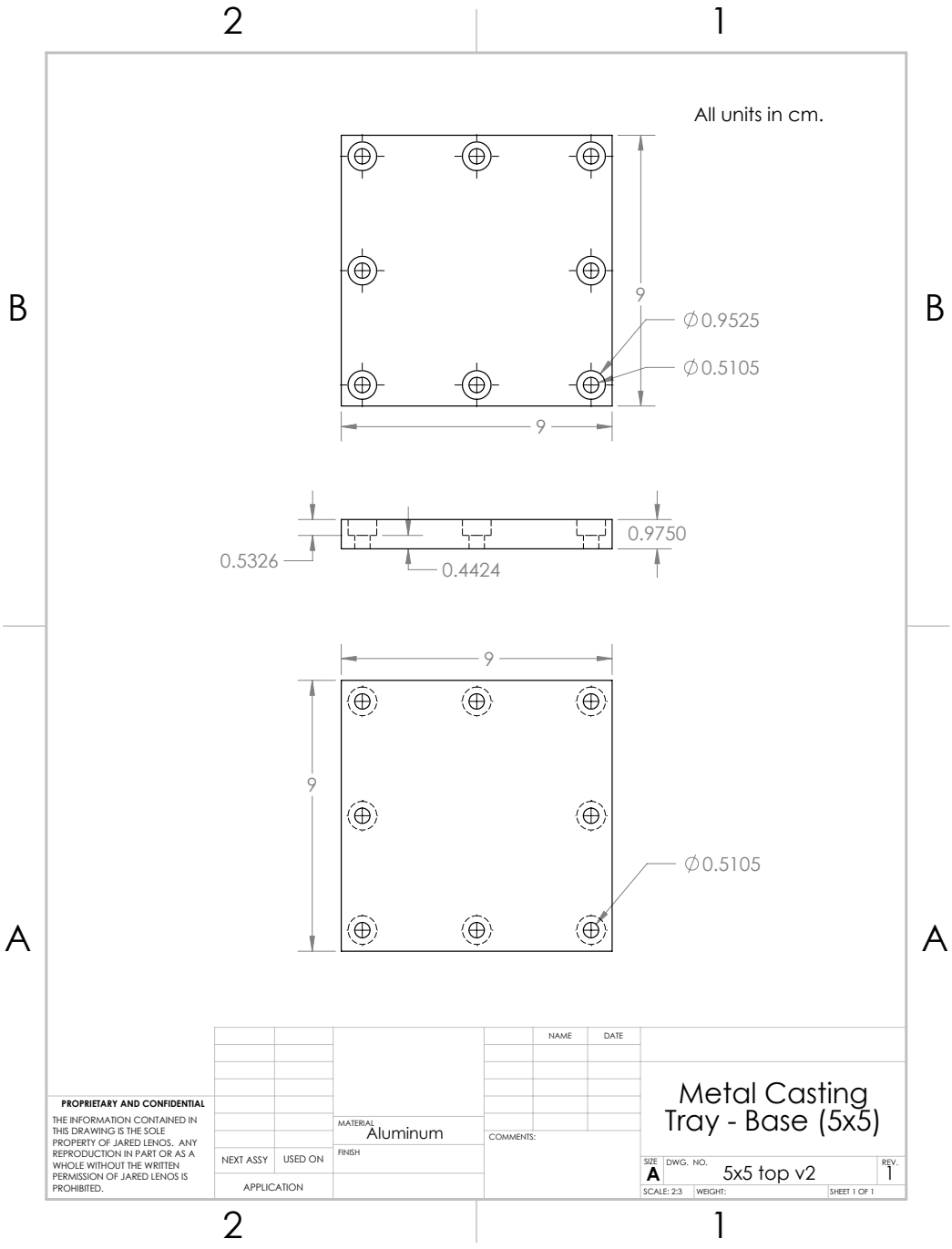

Figure A.2: Solidworks design of the 28.5 cm^2 casting tray bottom layer

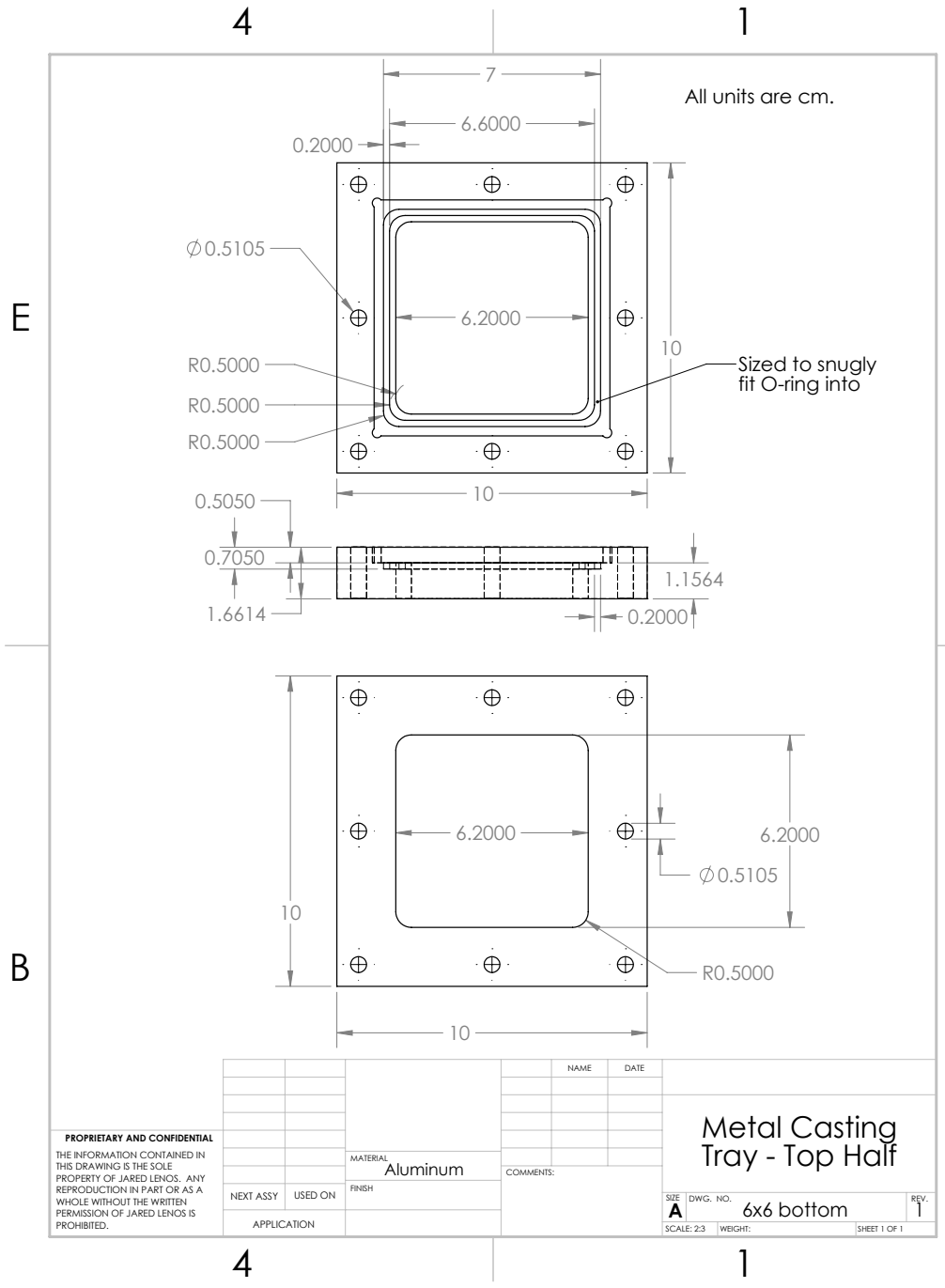

Figure A.3: Solidworks design of the 38.4 cm^2 casting tray upper layer

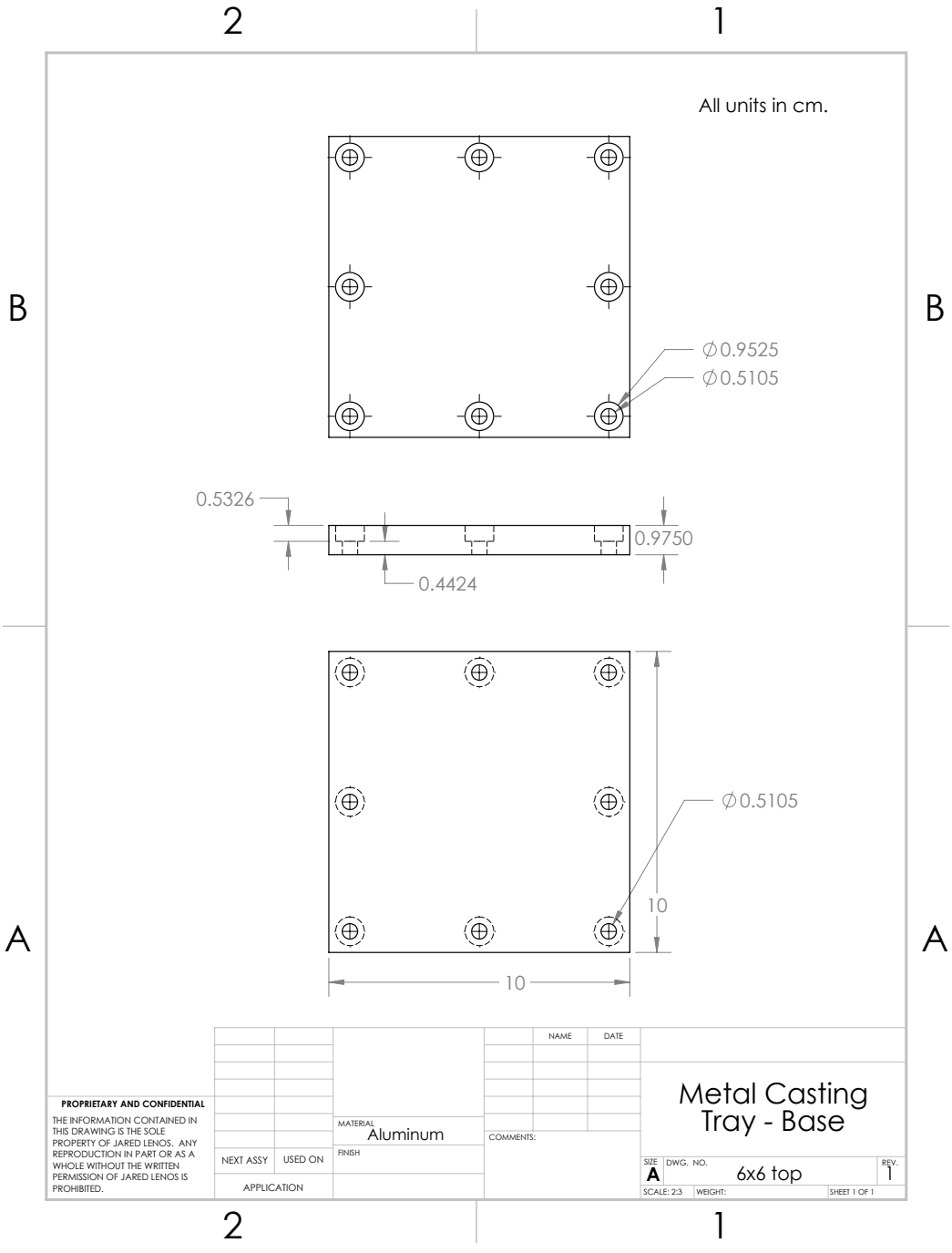

Figure A.4: Solidworks design of the 38.4 cm^2 casting tray bottom layer

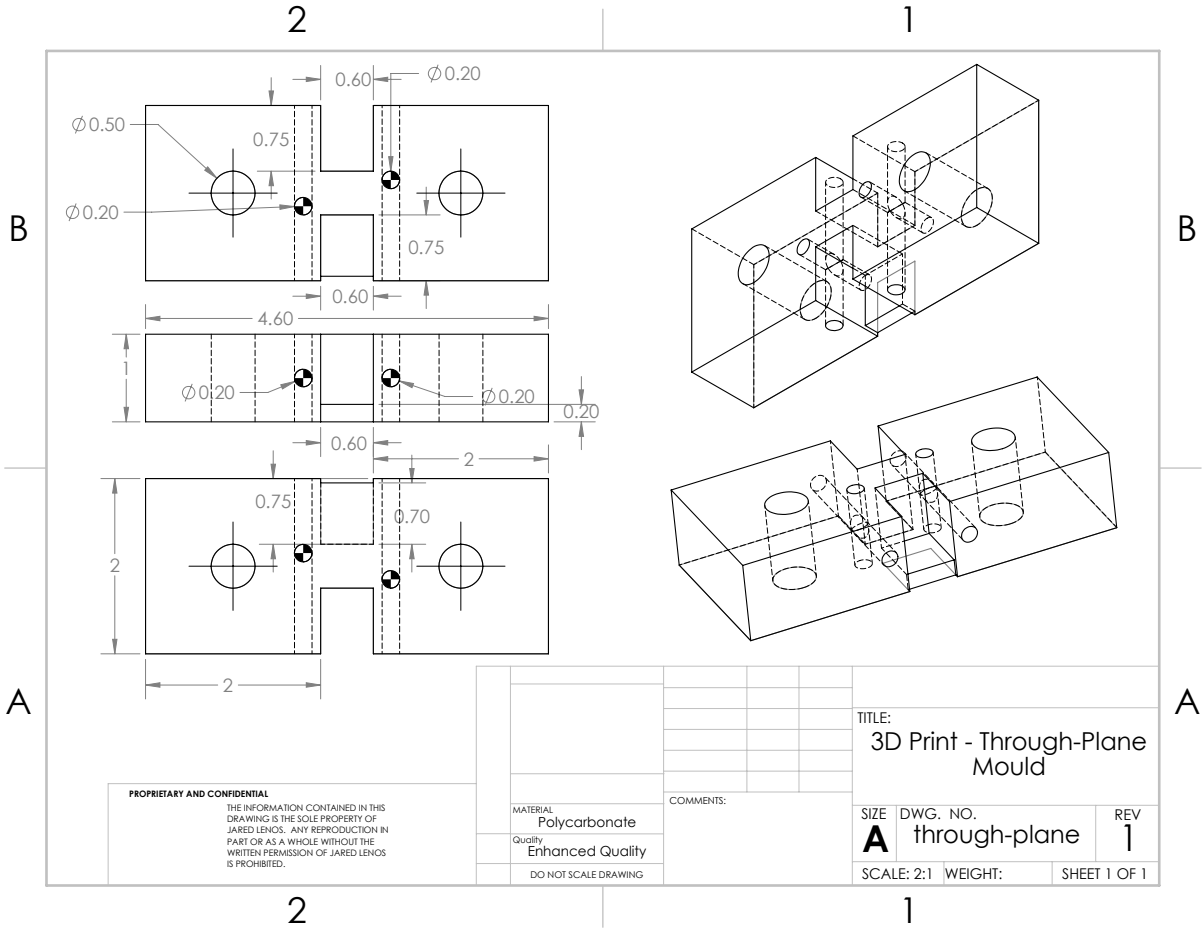

Figure A.5: Solidworks design of the through-plane measurement housing

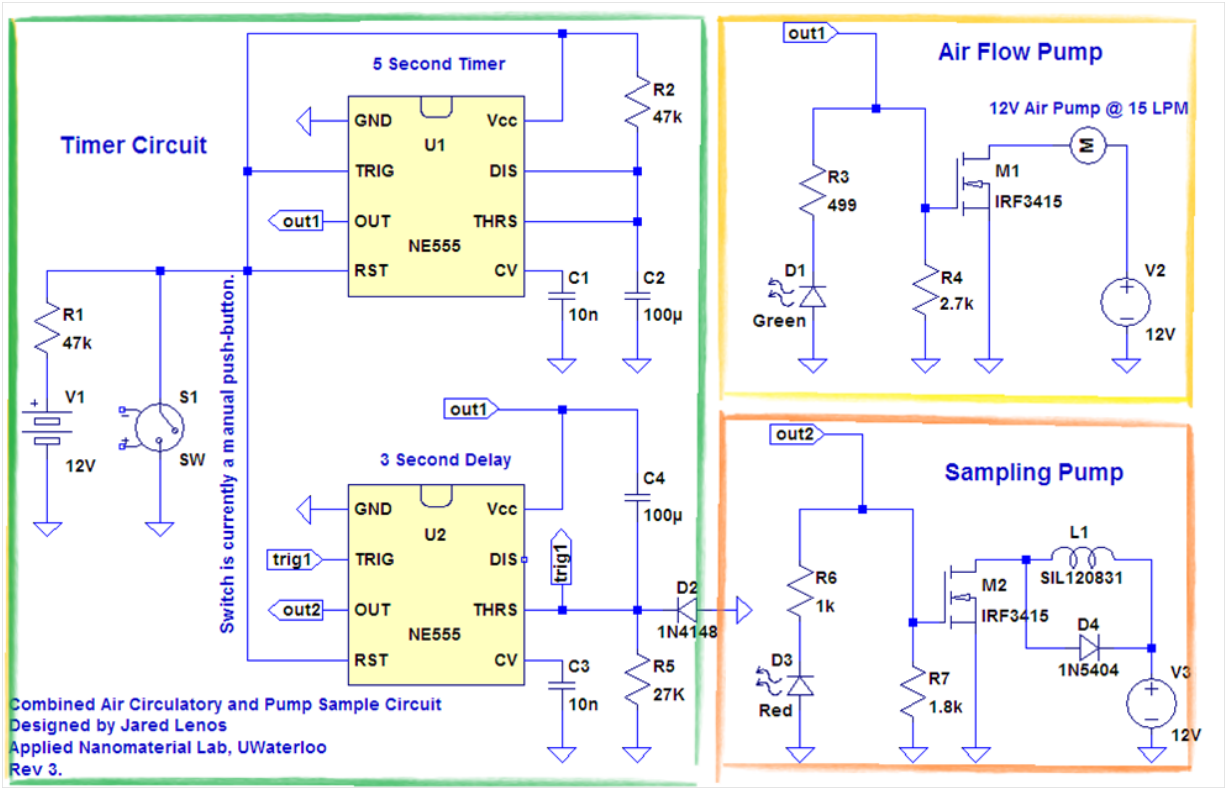

Figure A.6: Coupled fuel cell automated circuit [Green] Timer circuit design [Yellow] Air flow pump circuit [Orange] Solenoid sampling pump circuit

Appendix B

Tables for Comparison and Cost Analysis

Table B.1: Items, specification and price for the automated FCS setup

Product	**Product Code**	**Quantity**	**Price**
Units			CAD
Boxer Air Diaphragm Pump	3112-12V	1	USD 192.40
Electronics Science Shop	-	-	~30.00
Arduino Uno Microcontroller	RB-Ard-34	1	29.57
MOSFET N-Channel 150V/43A	IRF3415PBF	5	10.54
DC Power Adapter 12v/1A	DCA-1210	2	9.90
Breadboard 400 Tie Points	ZY-60	3	11.06
NE555P Bipolar Timer	NE555P	10	1.60
Red LED 3mm Diffused	LED3RD	20	0.63
AWG24 Insulated Copper Wire 8m	WIRE24	1	1.30
Subtotal			315.00
Shipping			17.16 & 54.85
Taxes			40.95
Approximate Total			400.00
Paid Total	Rest	--	359.98

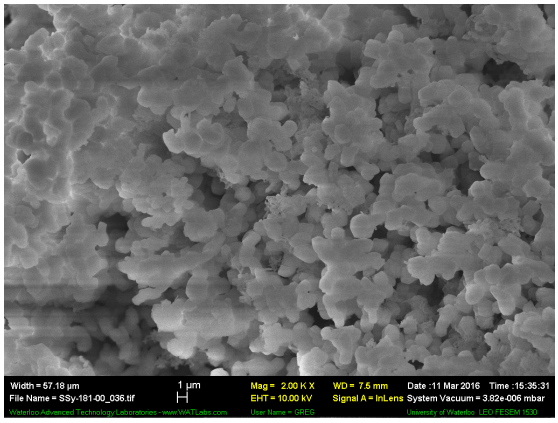

Figure B.1: 2K resolution of SBA-15 cubic structure

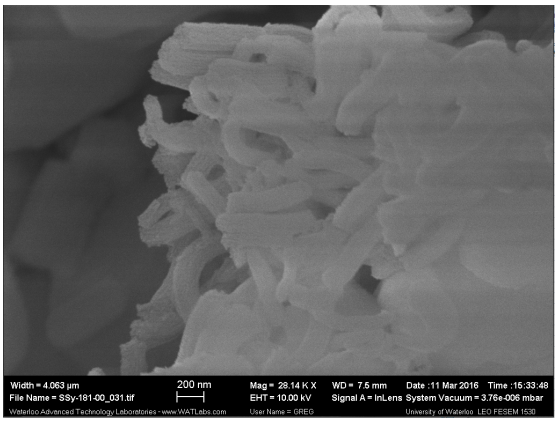

Figure B.2: 28.18K resolution of SBA-15 showing the nanosized porous structure

Table B.2: Chronological comparison of degredation test methodologies

Order Units	**Condition**	**Applied** ^{o}C/R.H. - Time	**Commercial** ^{o}C/R.H. - Time
1	Humidification	25/60 - 3 days	25/60 - N/A
2	1st Test	Ambient - 0.5 hr	Ambient - 0.5 hr
3	1st Bake	60/0 - 2 hr	60/0 - 2 hr
4	Rest Time	Ambient - 0.5 hr	Ambient - 1 hr
5	2nd Test	Ambient - 0.5 hr	Ambient - 0.5 hr
6	2nd Bake	--	60/0 - 2 hr
7	Rest Time	--	Ambient - 1 hr
8	3rd Test	--	Ambient - 0.5 hr
9	Storage	25/60 - Overnight	25/60 - Overnight
10	Day 2	Do 2-5 (2nd Bake)	Do 2-8 (3rd & 4th Bake)
11	Storage	25/60 - Overnight	25/60 - Overnight
12	Day 3	Do 2-5 (3rd Bake)	Do 2
13	Long Bake	--	60/0 - 4 hr
14	Rest	--	Ambient - 1 hr
15	Test	--	Ambient - 0.5 hr
16	Storage	25/60 - Overnight	25/60 - Overnight
17	Day 4	Do 2-5 (4th Bake)	Do 12-14 (6th Bake)
18	Storage	25/60 - Overnight	25/60 - Overnight
19	Day 5	Do 2-5 (5th Bake)	Do 2
20	Storage	25/60 - Until Needed	25/60 - Until Needed

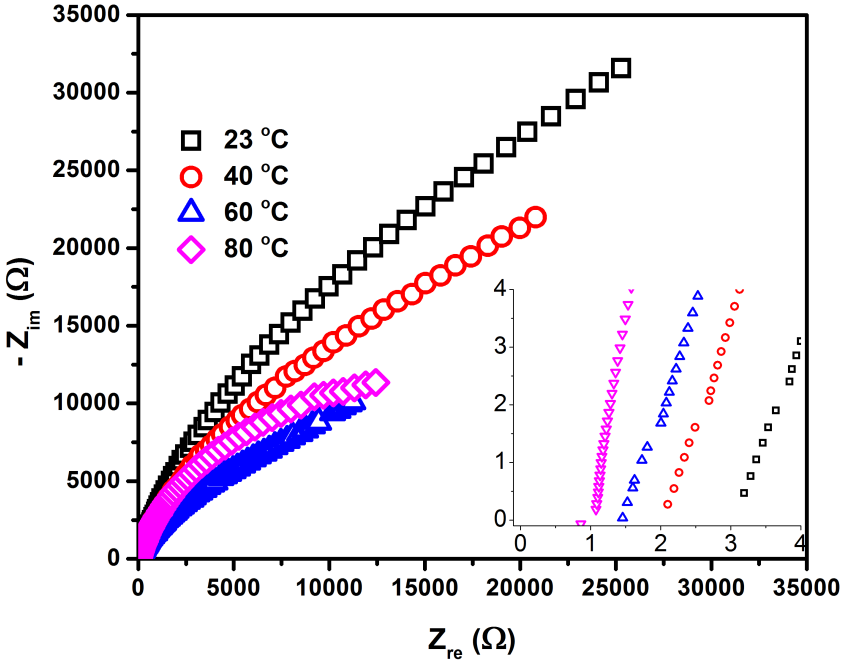

Figure B.3: Nyquist plots for ionic conductivity of a 50:50 SA-(SBA-15:GO) as a function of temperature at 100% RH

Appendix C

Code for Automated Data Analysis

Code C.1: Hardware controller switch code to interface between automated software and the benchtop testing hardware

```
//555 timer trigger- monostable mode
//by Jared Lenos
//March 2014

//pin connections:
//digital pin 0 to 555 pin 2
//Arduino ground to 555 ground (pin 1)
int go = 12; //Pin used to control MOSFET
int led = 13; //LED indicator light on board
//variable declaration
int cyclenum = 0;

void setup(){
  Serial.begin(9600); // initialize serial communication:
  Serial.println("Running_PEMFC, Author: JARED LENOS, March 2014");
  Serial.println("Email: <jared.lenos@gmail.com> if issues arise.");
  Serial.println();
  Serial.println("Welcome! Please send 'g' to run the attached hardware.");
  Serial.println("    ");
  pinMode(go,OUTPUT);
  pinMode(led,OUTPUT);
}

void loop(){
  if (Serial.available() > 0) {

    int inByte = Serial.read();
    // do something different depending on the character received.
    // The switch statement expects single number values for each case;
    // in this exmaple, though, you're using single quotes to tell
    // the controller to get the ASCII value for the character.  For
    // example 'a' = 97, 'b' = 98, and so forth:

    switch (inByte) {
    case 'g':     //Blink LED twice during one second before starting
      Serial.print("Commencing in");
      for(int i = 0; i < 2; i++)
      {
        Serial.print("\t");
        Serial.print(1-i/2.00);
        digitalWrite(led, HIGH);
```

```
        delay(250);
        digitalWrite(led, LOW);
        delay(250);
      }
      Serial.println("\t GO!");
      digitalWrite(go,HIGH); //drive MOSFET on
      delay(100); //give it 100ms to respond
      digitalWrite(go,LOW); //drive MOSFET off
      Serial.print("Air Pump ON \t");
      for(int i = 0; i < 6; i++)
      {
        digitalWrite(led, HIGH);
        delay(250);
        digitalWrite(led, LOW);
        delay(250);
      }
      Serial.println("Cell Pump ON");
      for(int i = 0; i < 14; i++)
      {
        digitalWrite(led, HIGH);
        delay(100);
        digitalWrite(led, LOW);
        delay(100);
      }
        cyclenum++;
        Serial.print("Cycle ");
        Serial.print(cyclenum);
        Serial.println(" complete.");
        break;
    default:
     // do nothing, make sure LED if off.
      Serial.println("That command was invalid.");
      digitalWrite(go, LOW);
      digitalWrite(led, LOW);
    }
  }
}
```

Code C.2: Script to interface between the Agilent DMM software and send output to the hardware controller

```
#IfWinActive Agilent BenchVue    ; Will only initialize script if the active window's class
    ↪                                matches.
#NoEnv                                ; Recommended for performance and compatibility
    ↪ with future                                AutoHotkey releases.
#SingleInstance Force             ; Instances run again will replace previous ones.
#HotkeyInterval 0
#MaxThreads 20                    ; Prevents possible crash.
#Persistent
#WinActivateForce                 ; Prevents window flashing if changing windows rapidly.
SetWorkingDir %A_ScriptDir%       ; Ensures a consistent starting directory.
SendMode Input                        ; Recommended for new scripts due to its superior
    ↪ speed and reliability.
SetBatchLines, -1
SetKeyDelay -1,-1
CoordMode, Mouse, Relative        ; Sets mouse clicks relative to the active window.
;Menu,Tray,Icon,%A_WinDir%\system32\shell32.dll,16

NumPass := 10                     ; Define Variables.
NumSec := 180
vFileName := ACS-Sample

;Add Tray Options
Menu, tray, tip, PEMFC AutoRun
Menu, tray, NoStandard
Menu, tray, add, Variables
Menu, Tray, add,
Menu, Tray, add, About
Menu, tray, add
Menu, tray, add, Exit

return

CapsLock::                        ; Use Capslock as a default initialization key.

        Gui, add, Text,, Please insert the file name you'd like to save results under.
        GUI, add, Edit, w400 vFileName
        Gui, add, Text,, Please insert the number of tests you will be making then press
            ↪ OK (Alt+O).
        GUI, add, Edit, w400 vNumPass, 10              ; 10 is set as the base number as
            ↪ a good                                                    sample should
            ↪  have this many.
```

```
        Gui, Add, Text,, Please insert the number of seconds between passes.
        Gui, add, Edit, w400 vNumSec, 180
        Gui, Add, Button, x180 y140 h30 w50, &OK        ; User Input section.
        Gui, -Theme
        Gui, Show,, PEMFC Autorun
        return
return

        GuiEscape:
        GuiClose:               ; If the users closes the window, prevents duplicate
            ↪ controls                                    being created.
        Gui, Destroy
        return

        ButtonOK:               ; Sends the program towards the loop cycle.
        Gui, Submit
        Gui, Destroy
        Goto Looping
        return

Looping:
{

        export_id := "HwndWrapper[Agilent BenchVue DMM.exe;;5b0b6434-7254-4adc-9869-
            ↪ e0c43bc177f9]"

        ClickXGo := 36
        ClickXStop := 130
        ClickY := 67
        CurrLoop := 0                   ; Counter to determine how long to wait.

Loop %NumPass% {
        WinActivate Agilent BenchVue    ; sets the Agilent program as the active window
        WinWaitActive Agilent BenchVue  ; waits for the program to be active
        MouseGetPos, xpos, ypos
        Click %ClickXGo%, %ClickY%, 0   ; Moves the mouse to the location on the screen
            ↪ for                                         'Start Test'.
        sleep 10
        Click %ClickXGo%, %ClickY%      ; Clicks to start the test.
        Click %xpos%, %ypos%, 0         ; moves the mouse back to where you had it before.
        Sleep 500
        Run, cmd /c echo "g">COM8,,Hide ; Sends "g" to the com port which is recognized as
            ↪  'GO'.
```

```
        ; Program sleeps until the software has finished reading.
        SleepTime := NumSec*1000+1500
        Sleep %SleepTime%

        ; After sleeping, end the data run, save the data and start a new run as quickly
            ↪ as possible.
        WinActivate Agilent BenchVue     ; sets the Agilent program as the active window
        WinWaitActive Agilent BenchVue   ; waits for the program to be active
        MouseGetPos, xpos, ypos
        Click %ClickXStop%, %ClickY%, 0 ; Moves the mouse to the location on the screen
            ↪ for 'Stop                                    Test'.
        sleep 10
        Click %ClickXStop%, %ClickY%     ; Clicks to stop the test.
        Click %xpos%, %ypos%, 0          ; moves the mouse back to where you had it before.
        sleep 1000                       ; Wait 1 seconds for 'Stop All' to progress.

        Click 1294, 632                  ; Export Button
        Sleep 500
        Click 1249, 597                  ; CSV choice
        ;;WinWait ahk_class %export_id%
        Sleep 1000
        Click 166, 80                    ; Wait for window to appear, click text
        Send ^a                          ; Select all text
        Send %FileName%                  ; Type in filename
        sleep 400
        Send {Tab 3}{Space 2}            ; uncheck number by twice on the number checkbox
            ↪ to make it auotmatically add a value to the data
        Sleep 400
        Click 33, 244                    ; Uncheck the "include setup text" box
        Sleep 400
        Click 460, 300                   ; Click OK to save data
        Sleep 40
        Click %xpos%, %ypos%, 0                 ; Move mouse back to its original position
        WinWaitActive ahk_class CabinetWClass   ; Wait for the windows explorer window to
            ↪ pop-up
        WinClose ahk_class CabinetWClass                ; Close the window
        CurrLoop++
}
WinActivate Agilent BenchVue             ; sets the Agilent program as the active window
WinWaitActive Agilent BenchVue           ; waits for the program to be active

If (CurrLoop = Numpass) {
MsgBox, 260, Script Continuation, Would you like to restart this entire cycle?
IfMsgBox Yes
```

```
        Goto Looping                    ; restarts the cycle if 'yes' is pressed.
        return
IfMsgBox No
        Goto Exit
        return
}
return
}

Variables:
Gui, Destroy
Gui, add, Text,, Please enter the sample name you would like to save.
GUI, add, Edit, w400 vFileName
Gui, add, Text,, Please insert the number of tests you will be making then press OK (Alt+O
    ↪ ).
GUI, add, Edit, w400 vNumPass, 10
Gui, Add, Text,, Please insert the number of seconds between passes.
Gui, add, Edit, w400 vNumSec, 180
Gui, Add, Button, x180 y140 h30 w50, &OK        ; User Input section.
Gui, -Theme
Gui, Show,, PEMFC Autorun
return

About:
Msgbox 64, PEMFC Autorun, Written for Agilent Benchvue by Jared Lenos.`nMarch 2014 @
    ↪ Applied Nanomaterials and Clean Energy Lab.
return

Exit:
ExitApp                                 ; Exit will end the running script.


Pause::Pause                            ; The script can be paused at any time by hitting
    ↪                                           'Pause'.
```

Code C.3: Script to automatically detect extrapolate and integrate response curves

```
/*
OriginPro 8.5 macro to generate results from data for the Ethanol Fuel Cell (PEMFC)

Description: This script is intended to automatically import, interpret and provide easy
    ↪ access to the information
that is necessary to properly analyze the DMM data collected from a single PEMFC fuel test
    ↪ . Essentially, it autom-
atically imports files, using their names to organize them. It then formats the current
    ↪ column to being in micro-
amperes, creates a line plot of a given sample, integrates that line from start to the 3/8
    ↪ ths and 3/4ths end point
and collects and displays the data for easy transferral to a final analysis tool.

Version: 1.5.1
Date: Mar 23, 2016
Contact: Jared Lenos <jared.lenos@gmail.com>
*/// NOTE: legendupdate mode:=custom custom:=@WS; // To quickly format legend entries in
    ↪ Origin.

/* Common import function and options to trim/rename sheets/books based on imported files.
    ↪  */

newbook;
string fns;
string path$=system.path.origin$;
int nLen = Len(path$);
path$=path.left(nLen-31)$ + "\Raw Data\2015\20150327\";
findfiles f:=fns$ e:="Com*.csv";
int n = fns.GetNumTokens(CRLF);
string bkName$=page.name$;
impasc fname:=fns$
options.ImpMode:=4                  /* start with new sheet */
options.Sparklines:=0               /* don't have sparklines */
options.Cols.AutoColTypes:=1        /* Origin automatically designs the columns */
options.Cols.NumCols:=2             /* only import the first 2 columns */
options.Names.AutoNames:=0          /* turn off auto rename */
options.Names.FNameToBk:=0          /* do not rename the workbook */
options.Names.FNameToSht:=1         /* rename sheet to file name */
options.Names.FNameToShtFrom:=0         /* trim file name from letter */
//options.Names.FNameToShtTo:=44                /* trim file name to letter */
options.PartImp.Partial:=1                  /* importing only these columns */
options.PartImp.FirstCol:=2
```

```
options.PartImp.LastCol:=3;
//options.Names.FNameToBkComm:=1       /* add file name to book comment */


newbook result:=SummarySheet;
wks.name$="Results";
for (ee=1; ee<=n; ee++) /* Runs as many times as the number of imports */
{

        win -a %(bkName$);              // Activates the book.
        page.active$=$(ee);             // Opens the page depending on the number of
            ↪ inputs.
        string wksname$=%(wks.Name$);   // Variable containing the name of the worksheet (
            ↪ from import).

        /* Change features of first column */
        Range a = 1;


        // Format column A to switch from a Date-Time to elapsed time.
        // - WARNING will screw up if going from 11 pm - 12 am.
        a=Right(Trim(a$)$,12)$;
        a.SetFormat(3, 11,);
        a=a*86400;
        a.Format=1;
        a=a-a[1];


/* Change features of second column */
        Range b = 2;
        b=b*1e6;                        // Format to micro-amperes
        b[L]$=Data (uA) ;       // Change Column Header info


// Figure out if a 'peak' exists in the first 10 seconds
// Find the index at which column A exceeds 10.
del -al partial;                // Delete temporary dataset it already exists.
int rangemarked = 0;
dataset partial;
for(ii=1; ii<=a.GetSize(); ii++) {
        partial[ii]=b[ii];
        if (a[ii] >= 10) break;
        }
int val2=ii;                    // Index at which the time exceeds 10 seconds.
```

```
// Build a temporary dataset
val=list(max(partial),partial);          // Index of the max value in in the 10 second
    ↪ window.
if (val < val2-4) {              // !! A peak value exists before the 10 second mark.
        int ii_next;                     //initialize a new variable for the 3rd forward
            ↪ point
        int bb_next;
        int bb=val;                      // initialize 'bb' at the peak to work backwards/
            ↪ forwards from
        for(bb=val-5; bb>=3; bb--)                                  // move backwards from the
            ↪  peak until a change is found.
        {
                bb_next = bb-3;
                if (b[bb_next]>b[bb]) break; //Check the point 3 values behind. If larger
                    ↪ there must be a sign change = point of inflection
        }
        for(ii=val+10; ii<=b.GetSize(); ii++)   // move forwards from this peak (may stop
            ↪ immediately)
        {
                ii_next = ii+10;
                if (b[ii_next]>b[ii]) break; //Check the point 10 values ahead. If larger
                    ↪ there must be a sign change.
        }
        //type $(bb);
        //type $(ii);
        startpnt=bb;
        endpnt=ii;
        range rr = b[startpnt:endpnt];
        mark -st rr;
        rangemarked = 1;
        }


// Do Sigmoidal fitting on the cuve and integrate for true area
range a = 1;
range b = 2;
range xx=3;
range yy=4;
endrow = a.nrows;
endtime = a[endrow];
step = endtime/(endrow-1);
xx[L]$="Time (sec)"; //longname of the x-column
xx.type = 4;     // set it to be an 'X' column
yy[L]$="Current (uA)"; //longname of the y-column
```

```
xx={0:step:1200}; // Extrapolate out to 1200 seconds.

dataset tmp=(b>=max(b))?1:0; // find max value
int ii=list(1,tmp); del -al tmp;
ii = ii+300; // Choose a point to start about 400 points past the initial peak.
range decaycurve = b[ii:end]; // Create a decay segment in the post peak area.

nlbegin iy:=decaycurve func:=logistic nltree:=tt; // initialize fitting the active plot
    ↪ using logistic model
//tt.maxiter=50;                // change some parameters
tt.tolerance = 1E-6; //change some parameters

nlfit; //fit to specified modele
yy=fit(col(3)); // apply fit to presented x-values
nlend;
del -al tmp;

xx=a; // Replace with original data for integration / graphing.
yy=b; // Replace with original data for integration / graphing.
baseline=yy[xx.nrows];  // Assume that the end of the dataset is the asymptotic value (ie.
    ↪  that decay happens by this time)
yy=yy-$(baseline);              // Subtact this baseline from the whole dataset (for
    ↪ comparison)

// Mask same data as in the original data */
//type $(startpnt); // Check the start & endpoints
//type $(endpnt);

if (rangemarked == 1) {
range rr = col(4)[startpnt:endpnt];
mark -st rr;
}

// Get the Decay Time value
range a=3; // Use the extrapolated dataset just incase the 3/8ths point was never reached
    ↪ in the original data.
range b=4;

val=list(max(b),b);     // Get index of max (b)
dd=max(b)*3/8;

// Start counting at 'val' to ignore values before the peak.
for(ii=val; ii<=b.GetSize(); ii++) {if (b[ii] <= dd) break;}
int val2=ii;
```

```
// Calculate difference
decaytime = a[val2]-a[val];

string bkname$ = page.name$;
string shname$ = layer.name$;

paMultiY iy:=[bkname$]shname$!(C,D) theme:="True Integral" clear:=0 append:=integrate ow
    ↪ :=[SummarySheet$]Results;

// Adjust data in the Results Spreadsheet
range realpeak=[%(SummarySheet$)]Results!col(7)[ee];
range datacol = [%(SummarySheet$)]Results!Col(1);
range indexcol = [%(SummarySheet$)]Results!Col(2);
range baselinecol = [%(SummarySheet$)]Results!Col(8);
range decaycol = [%(SummarySheet$)]Results!Col(9);
wcolwidth irng:=datacol width:=15;
datacol[L]$=Sample;
datacol[$(ee)]$=shname$;
indexcol[L]$=Dataset;
indexcol[$(ee)]=$(ee);
baselinecol[L]$=Baseline [uA];
baselinecol[$(ee)]=$(baseline);
decaycol[L]$=Decay Time [s];
decaycol[$(ee)]=$(decaytime);
}
```